The Effect of Satellite Observing System Changes on MERRA Water and Energy Fluxes

Franklin R. Robertson* NASA/MSFC
Michael G. Bosilovich NASA/GSFC/GMAO
Junye Chen U. Maryland/ESSIC and GMAO
Timothy L. Miller NASA / MSFC

To be Submitted to the AMS Journal of Climate
MERRA Special Issue

November 16, 2010

* *Corresponding address*: Earth Science Office, VP61, NASA / Marshall Space Flight Center, Huntsville, AL 35805, pete.robertson@nasa.gov

Abstract

Like all reanalysis efforts the Modern Era Retrospective Analysis for Research and Applications (MERRA) must contend with an inhomogeneous observing network. Here we examine the effects of the two most obvious observing system epoch changes, the Advanced Microwave Sounding Unit-A (AMSU-A) series in late 1998 and, to a lesser extent, the earlier advent of Special Sensor Microwave Imager (SSMI) in late 1987. These sensor changes affect model moisture and enthalpy increments and, thus, water and energy fluxes since the latter result from model physics processes that respond sensitively to state variable forcing. Inclusion of the analysis increments in the MERRA dataset is a unique feature among reanalyses that facilitates understanding the relationships between analysis forcing and flux response.

In stepwise fashion in time, the vertically integrated, global mean moisture increments change sign from drying to moistening and heating increments drop nearly 15 Wm^{-2} over the 30+ years of the assimilated products. Regression of flux quantities on an El Nino / Southern Oscillation (ENSO) sea-surface temperature (SST) index analysis reveals that this mode of climate variability dominates interannual signals and its leading expression is minimally affected by satellite observing system changes. Conversely, precipitation patterns and other fluxes influenced by SST changes associated with Pacific Decadal Variability (PDV) are significantly distorted. Observing system changes also induce a non-stationary component to the annual cycle signals.

Principal Component Regression is found useful for identifying artifacts produced by changes of satellite sensors, and defining appropriate adjustments. After the adjustments are applied, the spurious flux trend components are largely eliminated. Time series of the adjusted precipitation and the Global Precipitation Climatology Project (GPCP) data compare favorably

45 on a global basis. The adjustments also provide a much better depiction of precipitation spatial
46 trends associated with PDV-like forcing. The utility as well as associated drawbacks of this
47 statistical adjustment and the prospects for future improvements of the methodology are
48 discussed.

49

1. Introduction

Steady improvements in assimilated products has produced a legacy of important contributions regarding atmospheric dynamics (Dole, 1989; Simmonds and Keay, 2000; Thompson and Wallace, 1998, 2000; Thompson et al., 2000; Hoskins and Hodges, 2002), tropical water and energy fluxes, and climate variability on interannual time scales (Trenberth et al., 2000; 2001; 2008; Bove et al., 1998; Wang, 2002). Yet, as a tool for capturing decadal scale variability and detection of trends, the reliability of reanalysis products has yet to be realized (Bengtsson et al., 2004; Sterl, 2004). In part this is due to the fact that water, energy (and other) fluxes produced by the assimilation procedure are subject to uncertainties in the physical parameterizations. Perhaps more importantly, because our satellite observing system has been characterized by an evolving capacity to correct model state variables of heat, moisture and momentum on which the physical parameterizations critically depend, the fluxes determined from reanalyses contain variability that arises as a result of these discreet, aperiodic observing system improvements. In this paper we will examine how these observing system changes have affected the depiction of climate variability within the thirty plus year period covered by MERRA.

Bias correction methods developed since initial reanalysis efforts have significantly improved the consistency of more recent products. Dee and Todling (2000) used rawinsonde humidity data to correct slowly evolving background guess systematic error in the forecast model component of the GEOS data assimilation system. Andersson et al., (2005) were able to diagnose *a posteriori* the incompatibility of ECMWF model background dry humidities in cloud free areas with satellite moisture retrievals which ultimately resulted in increased rainout of assimilated water vapor and unrealistically high precipitation in the ERA-40 reanalysis. More

exacting demands to accommodate the monitoring of decadal climate signals and the growing but ephemeral mix of remotely–sensed data have spurred great progress in so-called "bias-aware" methodologies (Dee, 2005). Variationally-constrained bias estimation strategies have been developed (Derber and Wu, 1998; Dee, 2004) which embed the correction within the cost function minimization process (i.e. reconciling observations with the background guess). This allows the detection of time-dependent biases from the entire suite of observing systems (e.g. Dee and Uppalla, 2009). Like the JRA-25 and EC-Interim reanalyses (Onogi et al., 2007; Berrisford et al., 2009) the MERRA employs this bias correction approach.

Despite these advances, additional improvement in bias correction of data sets and models is still required as evidenced by the results of Trenberth et al. (2009) and Bosilovich et al., (2010) who highlight uncertainties in water and energy fluxes among the most recent reanalysis efforts. For example, net downward energy flux at the surface over oceans is approximately 14 Wm^{-2} for MERRA (but -18 Wm^{-2} for JRA) over the period 2000-2004 where modern remote sensing measurements should have the greatest impact. Global precipitation trends in MERRA exceed 0.5 mmd^{-1} or nearly 20% of the climatological global amount over this period, similar to the older ERA-40 reanalysis. In contrast, the EC-Interim reanalysis exhibits a *decrease* in rainfall of about 0.3 mmd^{-1} since 1990. Clearly, there are remaining issues not only with model physics inadequacies, but also their interactions with constraining data sets whose bias properties are varied and time dependent in nature.

Bosilovich et al. (2010) have presented a comparative summary of MERRA fluxes with those of other recent reanalyses and also highlighted the relationship between the MERRA trends and the initial availability of AMSU-A data. The goal of this paper is to provide a more detailed

96 characterization of these time-dependent biases and explore the efficacy of a statistical correction
97 strategy to reduce these artificial trends in water and energy fluxes. After reviewing the data
98 used in the study (section 2), we begin by analyzing the temporal variability of the water vapor
99 and heat budget increments and relate these forcings to the step-wise evolution in passive
100 microwave sensing associated with AMSU-A and SSMI (section 3). Section 4 provides some
101 diagnostics on what aspects of climate variability within the 30-year period survive or are
102 distorted by these artifacts. We then use principal component analysis to characterize space-time
103 variability of the increment terms. In section 5 we show how applying a statistical regression
104 methodology to identify and eliminate trend artifacts associated with satellite sensor changes
105 provides an effective correction. An assessment of the adjusted fluxes is presented in section 6
106 along with concluding remarks.

107 **2. MERRA data and diagnostics**

108 All data used in this study are monthly mean assimilated products taken from the MERRA
109 collection archived at NASA Goddard Earth Sciences Information and Services Center, GES
110 DISC, (http://disc.sci.gsfc.nasa.gov/). These include monthly mean vertical integrals of heat and
111 water budget components (tavgM_2d_int_Nx and tavgM_2d_int_Nx) and individual radiative
112 flux components (tavgM_2d_rad_Nx) for the period 1979 through 2009. These quantities at
113 their native resolution (0.50^o lat x 0.67^o lon) were regridded via box averaging to a 2.5^o lat x lon
114 grid to facilitate computing covariance statistics. More detailed documentation on the quantities
115 in these data sets can be found in the MERRA File Specification Document (Suarez et al. 2010).

116 From these data we can reconstruct the MERRA budget for enthalpy, $H \equiv c_p T_v$, written as
117

$$\frac{\overline{\partial H}}{\partial t} = \overline{Hfluxconv} + \overline{\omega\alpha} + MST_H + RAD + SENS + ANA_H + Res_H \quad (1)$$

where c_p is the heat capacity of dry air at constant pressure and T_v is the virtual temperature. Overbars denote a vertical integration over the mass of the atmosphere and the subscript H denotes reference to the virtual enthalpy budget. The first two terms on the right hand side of (1) represent the convergence of enthalpy and the release of total potential energy, the global integral of the latter being equivalent to the generation of kinetic energy. The other tendencies involve moist processes (MST_H, which is essentially precipitation), radiative heating (RAD), and turbulent diffusion (i.e. sensible heat flux, SENS). The analysis increment (ANA_H) is the tendency that is added to the prognostic budgets due to the observational analysis. Res_H is a small value that includes the gravity wave drag and a residual that results from maintaining energy balance in the presence of numerical dissipation, each of which are also included in the output diagnostics (Suarez et al., 2010).

The vertically integrated radiation heating term, RAD, can be expanded further into the difference of top of the atmosphere, TOA, and surface shortwave fluxes (SW_T and SW_S, respectively) minus the sum of outgoing longwave radiation at TOA (OLR) and the net longwave flux to the surface, LW_S:

$$RAD = (SW_T - SW_S) - (OLR + LW_S)., \quad (2)$$

The MERRA vertically integrated total water vapor budget can be written as:

$$\overline{\frac{\partial q_v}{\partial t}} = \overline{qfluxconv} + MST_q + EVAP + ANA_q + Res_q, \quad (3)$$

where the change of water vapor is related to the dynamical convergence of water vapor, the net moist physical processes, MST_q, essentially the negative of the sum of convective, large-scale and frozen precipitation since precipitation is a sink of water vapor, and evaporation, EVAP. Here the subscript q denotes reference to the water vapor budget. Note that $-(L/c_p)MST_q = MST_H$. Two non-physical terms affect the moisture budget. ANA_q represents the analysis increment of water vapor and Res_q represents a very small amount of negative filling, ensuring positive water vapor content.

3. MERRA T, q increments and their evolution

In this section, we examine the statistical properties of the MERRA vertically-integrated moisture and temperature increments, focusing in particular on signatures of satellite impacts. Climatological mean maps of the moisture and heating increments are presented in Figure 1. It should not be surprising that the moistening and heating increments have systematic spatial structure to them since model physics deficiencies vary as a function of climate regime. In general, positive moisture increment values maximize over the tropics, most notably in the NH Summer warm pool areas (western Pacific, northern Indian Ocean, and Inter-American Seas). These are preferred areas of deep moisture and frequent convection (Adler et al., 2003) and the added moisture from the increments is acting to systematically increase precipitation (not shown). There are also positive values in oceanic subtropical ridge locations in eastern ocean basins where precipitation is quite small but the transition from stratocumulus to trade wind cumulus regimes are found. In the eastern Pacific a region of negative increments (drying) just

164 south of the equator forms a pronounced dipole structure with the positive values lying
165 immediately to the south. In the region of negative moisture increments boundary layer air over
166 the cold upwelling water off the coast of South America is systematically too wet in the
167 background field. Presumably these features indicate that the delicate interplay between
168 subsidence drying and shallow convective moistening of the equatorward moving airmasses is
169 not handled as well in the model as it should be.
170
171 Heating increments are predominantly positive over the continents and adjacent waters with
172 an equatorially symmetric cooling pattern over the central subtropical Pacific. The fact that the
173 moisture and heating increments have such different spatial patterns indicates that dynamical
174 transports of heat and moisture significantly affect the thermodynamic adjustments. The off-
175 equatorial cooling pattern is reminiscent of Rossby modes emanating from forced heating over
176 the western Pacific (Gill, 1980; Hoskins and Karoly, 1981) where ANA_q has a relative
177 maximum. One possible explanation for this structure is that the precipitation and associated
178 Gill-like dynamical heating response, poleward and downstream of the heat source, is somewhat
179 excessive compared to reality. This is consistent with the comparisons to GPCP precipitation
180 shown by Bosilovich et al., (2010). The extra heating would then require a systematic cooling
181 increment in order for the analysis to match satellite radiances.
182 Given a uniform observing system, ANA_H and ANA_q would be essentially stationary in a
183 statistical sense with some constant bias owing to model physics deficiencies[†]. Unfortunately,

[†] Complicating this is the fact that we also expect the analysis increments to have some sensitivity to climate variability. In section 5 we will see that ENSO may systematically perturb the GEOS-5 model climate and thus introduce some systematic variation in the flux bias.

this is not the case in reality due to the significant stepwise evolution of the satellite observing system. Figure 2 presents Hovmoeller plots of zonally-averaged ANA_q and ANA_H anomalies for the 1979-2009 period. (Henceforth, all anomaly quantities are understood to be departures from their monthly-varying seasonal climatology defined by the period 1979-2009.) From this perspective discontinuities in the increments resulting from the discreet changes in the observing system are now evident, particularly for ANA_q. The most obvious of these is the abrupt change to positive moisture forcing in November 1998 when the assimilation of NOAA15 AMSU-A radiances begins. This moistening is prominent at tropical latitudes and also over the Southern Oceans. Also apparent is the effect of the SSMI sensors whose data begin in late 1987 and which tend to decrease the drying from other observations in the tropics, but dry the high latitudes, particularly in the SH. The increasing amplitude of the apparent SSMI-induced changes over the Southern Ocean likely results from the increasing number of those sensors deployed with time during the 1990s. Presumably the SSMI and AMSU-A effects in the NH are muted because of the far denser conventional observing system there compared to the SH and tropics.

The ANA_H change associated with the onset of AMSU-A data ingest is prominent, particularly in the equatorial region and in the southern hemisphere. It is evident that as the moisture forcing increases with time in these regions, heating increments generally trend in the opposite direction; less heating is needed to keep the analyzed temperature consistent with observations. Beyond this first order change in ANA_H with time series, other features are also noted such as the presence of "blockiness" or discontinuities of multi-year duration in the northern hemisphere, particularly poleward of 30^o N. It is not clear why these shorter duration

features should occur in a relatively data rich portion of the globe. It is possible that surface emissivity uncertainties affecting the assimilation of the 50.3 GHz window channel (MSU CH1 and AMSU-A CH 1-3 and 15) could vary from sensor to sensor in such a way as to affect the inference of atmospheric temperature, but the explanation of these patterns will require more in-depth analysis.

The presence of annual cycle power in both increments despite the removal of the respective mean values over the reanalysis is also striking and indicates variations both in amplitude and in phase. After the buildup of SSMI sensors beginning in 1987 the increments near 50^{o} S have a maximum drying in SH Winter (JJA); yet after the AMSU-A ingest begins, a dramatic SH Winter moistening is evident. A summer heating / winter cooling cycle in ANA_H centered south of 45^{o} S also reverses phase after the start of AMSU-A data. Another shift in the annual variation of ANA_H begins in the northern hemisphere in 1998 and strengthens substantially in 2002. Clearly, the changes in sensors are associated with changes in the required annual cycle of forcing. For purposes of climate analysis this is a complicating factor.

All of these structures noted here emphasize the important interactions of a changing observing system interacting with a model having its own specific hydroclimatic biases. To explore the origin of these discontinuities further we turn first to monthly mean statistics of observation-minus forecast (OMF) and observation-minus analysis (OMA) residuals for the various AMSU-A channels of the NOAA polar orbiting suite. Simulated radiances based on the model 6h forecast and analyzed fields are generated using the forward observation operator of the CRTM (Han et al., 2006). The difference between the monthly mean values of OMF and OMA residuals, in turn, provides an estimate of the monthly mean contribution of the radiance

increments (AMF) in observation space. Figure 3 shows time mean maps of AMF from 1999 to 2002 for NOAA 15 AMSU-A Channel 15, one of the AMSU-A window channels (1, 2, 3, 15) sensitive to water vapor and liquid water emission, and for Channel 5, the oxygen absorption channel sensitive to mid- and lower-tropospheric temperature and surface temperature and emissivity. It is primarily through the window channels that the AMSU-A instrument can affect the water vapor increments. Over ocean the Channel 15 AMF pattern shows a strong resemblance to various features of climatological moisture increment pattern in Figure 1 with significant amplitude over the northern Indian Ocean / Warm Pool region, along the South Pacific Convergence Zone, and around the Gulf of Mexico and surrounding regions. The AMF values in Channel 5 have a pattern of cooling over the NH Summer warm pool position—consistent with the heating increment Hovmoeller plot in Figure 2.

Over land, where the window channels are sensitive to surface emissivity variations, the signals of both channels are quite large. In MERRA, the window channels are assimilated over land also, but only for footprints which can be classified as having a single surface type (i.e. mixed land / water or ice-covered / ice-free points are eliminated). We suspect that because of the far denser conventional observation network over land, the increment contributions from these channels end up having much less impact on the increments ANA_q and ANA_H. However as noted in the discussion of Figure 2, there is some evidence to suggest that their effects on temporal variations over land are not negligible.

Confirmation of the central role AMSU-A window channels play in producing a change in the moisture increments is demonstrated in an assimilation experiment in which the window channel data are withheld from the assimilation (Figure 4). Within two weeks of the onset of

253 AMSU-A data assimilation (Nov 2, 1998) the moisture increments in MERRA have led to
254 systematically larger precipitation (~ 0.1 mm d^{-1}) compared to the experiment in which these
255 moisture-sensitive channels are withheld. This result is comparable to that from an experiment
256 in which all AMSU-A channels are withheld (not shown). Accounting for the radiometric
257 warming of the window channels by liquid water (after removal of likely precipitating footprints)
258 is necessary to correctly interpret the observed radiances in terms of water vapor present. A
259 second experiment in which the window channels are retained but the standard bias correction
260 for liquid water is eliminated results in an even larger forcing of precipitation than seen in
261 MERRA. This illustrates the importance of the liquid water correction and raises the question of
262 whether the present correction in MERRA is sufficiently accurate. Other possible causes of
263 these artifacts might include differences in the way the cross-track scanning AMSU-A and the
264 conical scanning SSMI instruments detect vertical moisture structure, or perhaps its ensuing bias
265 correction. A full analysis of these issues is beyond the scope of the present paper but is the
266 subject of ongoing investigation. Regardless of the ultimate cause, there is strong evidence here
267 that the problem begins with non-physical moisture forcing changes leading to condensation and
268 heating increment changes.

269 **4. Modes of variability in MERRA**

270 *a. Globally-averaged time series*

271 The presence of these discontinuities in the ANA_q and ANA_H forcing, and their demonstrated
272 relationship to the microwave components of the satellite observing system, naturally raises
273 concerns regarding the ability to detect real variability in the climate system from MERRA. In
274 this section, we present an analysis of the major modes of variability in the vertically-integrated

MERRA water and energy budget variations in terms of global means over separate ocean and land areas (Figures 5 and 6)**.** The water vapor increment and precipitation[‡] in Figure 5 are strongly correlated over ocean and are the largest terms in the moisture balance equation. Note that the time-mean moisture increment is small over ocean but the increment changes sign dramatically beginning in Nov1998 when N15 AMSU-A assimilation begins. Moisture convergence and evaporation also respond in time with the increment and decrease over the oceans after AMSU-A enters the data stream in Nov1998. Moisture transport from ocean to land thus increases at this time. Over land the predominant balance is between increasing moisture convergence and precipitation anomalies with the increment playing a much smaller role. The moisture increment correlates negatively with moisture convergence suggesting that over land the influence of the moisture transport from oceanic regions runs counter to the conventional observations over land.

Especially prominent in the over ocean budget is an annual cycle component. Despite the removal of a mean annual cycle over the 30-year record, Figure 5 provides evidence of non-stationarity at this frequency. These signals change phase over the 30-year period.

The most prominent aspect of the enthalpy budget in Figure 6 is the negative correlation between the heating increment and precipitation over ocean. This is consistent with the interpretation that as moisture increment forcing increases, it triggers more precipitation and so less net atmospheric heating is needed to force the model temperature to agree with the observations. From this global perspective the stepwise increases in moisture increments appear

[‡] MST in the MERRA archived data is the net moisture source due to moist physics which is essentially precipitation and is negative in the moisture budget and positive in the heat budget. Thus, the budget terms are all additive in the sense of contributing to positive q_v and T_v tendencies.

295 to be the driving mechanism. However, the enthalpy increment has a more complicated step-like
296 structure than does the moisture increment and the upward precipitation steps in late 1987 and
297 1998 are less obvious in the heating increment. It is also possible that other factors such as inter-
298 calibration uncertainties of the MSU and AMSU temperature sounding channels may be
299 inducing additional increment changes that complicate the signal.

300 Like the precipitation heating, dynamical heat transport has strong variations with power at
301 the one year time scale which results from heating increments that have changing phase and
302 amplitude. These are particularly dominant over land. Note that for both moisture and heat, the
303 increments over land are strongly anti-correlated with the dynamical transports, indicating that
304 increment-induced precipitation heating changes over the ocean lead to circulations and
305 transports that must be compensated over land to keep T_v and q_v near observed values there.
306 Sensible heat flux variations are small and unremarkable averaged over global domains but in the
307 following section we will note significant regional variability.

308 For averages taken over ocean and land areas *at the global scale* the trend and non-stationary
309 annual cycle signals appear to completely dominate any physical variations that might be present
310 on interannual and longer time scales.

311

312 *b. EOF Analysis*

313 For convenience as a diagnostic, we have also used principal component analysis (PCA) to
314 extract major patterns of coherent variability in exploring the analysis increments, ANA_q and
315 ANA_H. The leading five EOF patterns and principal components (PCs) for ANA_q and ANA_H are
316 presented in Figures 7 and 8 and explain roughly 30 and 40%, respectively of the monthly

317 variance after the climatological mean plus annual cycle are removed. (Note that the product of
318 the EOF and principal component time series of a given mode produce the contribution of that
319 mode to the total anomaly signal.) The leading EOF of the moisture increment has as its primary
320 signal the increase in water vapor forcing over the northern Indian Ocean, tropical Pacific, and
321 inter-American Seas. Variations in the phase and amplitude of the annual cycle dominate the
322 second mode and relate to the pre-SSMI and AMSU-A epochs. The third mode most clearly
323 captures the tropical moistening and southern ocean drying as the number of SSMI sensors
324 grows after Aug 1987, and then the near reversal of this forcing with the beginning of AMSU
325 data. For the enthalpy budget, the leading trend mode carries the signal of decreased (increased)
326 heating over the Warm Pool and western Pacific (eastern Pacific) with time. Other modes
327 modify the linearity of this trend.

328 In both ANA_q and ANA_H, each of the modes has superimposed on it signals of evolving
329 departures from a mean annual cycle. These features change both phase and amplitude between
330 the pre-SSMI and ATOVS epochs as discussed in connection with Figure 2. These signals of
331 non-stationarity are also present to a smaller extent in the remaining modes we have not shown.
332 Although most of the dominant signals in both increments are found over the global oceans,
333 there are also significant centers of action over land. The moisture increments over land are
334 largely confined to the southern hemisphere while heating increments are present over northern
335 hemisphere land areas as well. Central Africa is an area of particular interest; Bosilovich et al.
336 (2010) have shown that strong decreases here in MERRA precipitation, evaporation and
337 moisture convergence occur after 1995 in conjunction with a change in equipment at radiosonde
338 station Bangui, (Station ID 64650). They also show that GPCP precipitation gives no indication
339 of the drop seen in MERRA precipitation. The leading mode of ANA_q (Figure 7) indicates a

340 change in sign from negative to positive in moisture forcing in central African as the AMSU
341 sensors become available after 1998. We suspect that the onset of more moisture data with the
342 window channels may enable the analysis to partially combat the erroneous drying produced by
343 the radiosonde instrumentation change.

344 While PCA is able to isolate a large fraction of the variability associated with sensor changes,
345 one cannot say that a given mode reflects a specific sensor change. It is important to remember
346 that, by construction, the orthogonality of the successive EOFs is purely a mathematical
347 property. Nevertheless, the PCA diagnostics presented here highlight the discrete temporal
348 discontinuities in the MERRA budget terms and, by virtue of their coincidence with sensor
349 changes, illustrate the dominance of the sensor-related artifacts in explaining the total variance of
350 the increments.

351 *c. Interannual and near-decadal signals*

352 Given that a large fraction of the interannual to decadal variability in monthly mean flux
353 anomalies can be explained by the effects of the AMSU-A and SSMI observations entering the
354 data stream, what are the implications for the utility of MERRA in terms of climate variability
355 within the period analyzed? The El Nino / Southern Oscillation phenomenon is the largest
356 globally coherent variability signal in the climate system. To determine whether this signal can
357 be extracted despite the trends in the data we have regressed the monthly flux anomaly fields
358 against an ENSO SST index. Our base SST time series is constructed using the Extreme Least
359 Lag methodology (Chen et al., 2008a) which varies similarly in time with Nino 3.4 SST but also
360 accommodates both positively and negatively lagged SST anomalies over the global oceans. The
361 results of regressing the moisture and heat flux anomalies against the time series of this globally

362 averaged index, normalized by its standard deviation of 0.061 K are shown in Figure 9. Clearly,
363 the precipitation patterns (-MST_q or MST_H) agree closely with well-known indices of ENSO
364 induced rainfall anomalies (Ropeleski and Halpert, 1987; Curtis and Adler, 2000). Increased
365 precipitation over the equatorial central and eastern Pacific with suppressed precipitation over
366 the Maritime continent and South Pacific Convergence Zone is well captured in the reanalysis.
367 Teleconnected precipitation anomalies over the Amazon and Indian Ocean regions are also quite
368 realistic. Radiative heating anomalies associated with the precipitation patterns capture the
369 anomalous heating in the precipitation regions and the increased energy loss via OLR in the
370 surrounding subtropics and tropical region west of the dateline. The former is due principally to
371 increased greenhouse effects of water vapor and clouds while the latter is due to a warmer
372 radiating atmosphere with somewhat enhanced aridity combining to enhance OLR in anomalous
373 subsiding regions. Both moisture and heating dynamics terms indicate the strong role in
374 bringing moisture to regions of anomalously large precipitation and supporting the release of
375 potential energy through anomalous vertical overturning. The latent heat flux exhibits a complex
376 pattern with double maxima in the eastern tropical Pacific and broadly negative values west of
377 the dateline and over the subtropical North Atlantic Ocean. Both changes in wind speed and
378 near-surface moisture anomalies act to produce this complex pattern. Sensible heat flux
379 anomalies are largest over land and show elevated values in the Australasia region and Amazon
380 basin; these are areas well-known to have excessive aridity during warm ENSO events. Reduced
381 sensible heat fluxes are found in eastern equatorial Africa associated with elevated cloudiness,
382 precipitation and reduced solar forcing during warm ENSO events. Additional future studies can
383 examine these gross patterns in more detail—e.g. aspects of the lag relationships between SSTs
384 and fluxes, the asymmetry of warm and cold events, and details of energy transformations and

385 transports. Our point here is just to show that despite the pronounced trend in many of the
386 fluxes, coherent relationships between SST variations and the regional flux patterns on the
387 interannual scale appear to remain intact.

388 The relatively high frequency of ENSO (2-7 years) allows effective separation of the SSTs
389 and flux signals from the trend signal; furthermore, in the case of ENSO the signal is well
390 known, *a priori*. For lower amplitude, lower frequency variations in fluxes the problem becomes
391 more difficult. For example, Pacific Decadal Variability (Zhang et al., 1997; Deser et al., 2004;
392 Chen et al., 2008b; Burgman et al., 2008) is a well-known low-frequency mode of behavior that
393 produces systematic variations in precipitation, radiation and circulation in conjunction with
394 broad changes in SST structure over the Pacific basin. Figure 10 shows the leading SST EOF and
395 PC after the ENSO signals have been removed from the data during the 1979-2009 period via the
396 method of Chen et al. (2008a). After performing an EOF analysis on this filtered SST data, the
397 first mode contains the bulk of the PDV signal. There is the characteristic trend of cooler water
398 over the eastern Pacific and the horseshoe-like increase in SST in the western subtropics of both
399 N and S hemispheres. Note that some signature of the Atlantic Meridional Overturning
400 (Schlesinger and Ramankutty, 1994; Enfield et al., 2001) and the cooling induced by the Mt.
401 Pinatubo eruption are also present. Some of the trend in this PC is also related to the century-
402 scale rise in SST, but overall the PDV signal dominates regional trends. Also shown in Figure
403 11 are GPCP and MERRA precipitation anomalies regressed onto this PC. The GPCP
404 precipitation pattern is very similar to that reported by Burgman et al. (2008) in an observational
405 analysis of PDV. The MERRA patterns bear some similarity in the large scale patterns but
406 notable differences such as those in the Indian and central Pacific Oceans are prominent. Clearly
407 the non-physical long-term trend signal in MERRA gets picked up in the regression procedure.

While no thirty-year reanalysis is long enough to truly quantify decadal scale variability, low frequency variability patterns *within* the satellite era are distorted in MERRA by the satellite-related artifacts.

5. A Statistical Adjustment Methodology

Is it possible to adjust the fluxes in any defensible way, so as to minimize these artifacts? One might argue that simply removing the trend modes by means of the EOF analysis would be useful, but these modes explain only a portion of the detectable sensor change signal—it is not linear. Furthermore, additional analysis of the EOF decomposition of the fluxes (not shown) indicated that for many terms the trends are mixed with real variability (e.g. the ENSO signals). Attempting to remove these modes would damage real signals of variability.

A more viable approach is to use the leading modes of ANA_q and ANA_H discussed above to remove the artifacts in the fluxes by linear regression, that is, projecting the flux data onto the PCs of the individual increment modes and then removing these components from the fluxes. This technique is commonly referred to as principal component regression (PCR). Conceptually, the vertically-integrated equation for moisture or enthalpy can be written as

$$\frac{\partial X}{\partial t} = \sum_{i=1}^{n} F_i + I_x \qquad (4)$$

where X is moisture or enthalpy, F_i is any one of n physical terms (e.g. surface and TOA fluxes and dynamical transports), and I_x is the moisture or enthalpy increment. All quantities are understood to be vertically-integrated, mass weighted departures from their respective monthly-resolved climatologies.

We can formulate an adjusted physical budget term as

$$F_i^* = F_i - \sum_{j=1}^{m} \hat{\mathbf{F}}_{i,j} PC_j \quad (5)$$

where the $\hat{\mathbf{F}}_{i,j}$ are the spatial vectors of regression coefficients of the ith budget term on the PCs of the m leading increment modes. The PCs have only temporal variability.

We also formulate a modified increment,

$$I_x^* = I_x - \sum_{j=1}^{m} \hat{\boldsymbol{I}}_j PC_j \quad (6)$$

which is composed of the original increment minus the sum of m modes, each of which is composed of the EOF spatial vectors $\mathbf{I}_j$ multiplied by their respective principal components, PC_j.

The adjusted budget equation now reads

$$\frac{\partial X}{\partial t} = \sum_{i=1}^{n} F_i^* + I_x^* \quad (7)$$

where the modified increment and the physical terms are now free of the leading modes that relate to the satellite artifacts.

Of course, one potential drawback to this procedure is that we are subjectively declaring which subset of increment modes are affected by artifacts. In general, we cannot expect all of the artifact-related variability to be collected into just a few modes. It is also likely that some physical variability will project to some extent onto the modes we select, mixing with the non-physical signal. As noted earlier, removing sensor change effects from the fluxes is complicated by the fact that we also expect the analysis increments to have some sensitivity to climate variability (e.g. ENSO or other events that systematically perturb the distribution and intensity of precipitation and radiation).

448 The methodology outlined here is closely related to Redundancy Analysis (von Storch and
449 Zwiers, 1999; Wang and Zwiers, 2001; Bakalian et al., 2010), a variant of several techniques
450 widely used to find covariability between two datasets. Like canonical correlation analysis,
451 CCA, Redundancy Analysis (RA) finds a hierarchy of paired modes, predictors and predictands,
452 that maximize some metric of variability. But rather than maximizing correlation, RA
453 maximizes the explained predictand variance and associates that with a predictor mode. We
454 performed the analysis with both RA and PCR methods, with virtually identical results.

455 Based on examination of the increment EOFs and PCs we selected five PCA modes from
456 each of the increments to define the artifact signals. These were the first four and the seventh
457 moisture increment modes and the first five enthalpy increment modes. Experimenting with
458 variations on this selection showed that the first three modes of each increment are crucial and
459 that using more than 10 modes began to weaken the retained variance noticeably.

460 In centering the data for the regression analysis, we must define an annual cycle and mean
461 values. We have opted to use the entire record from 1979 onward to define the climatology,
462 because choosing any shorter period might not yield adequate sampling of the annual cycle.
463 Obviously this is subjective and one could argue that the most recent period with the most robust
464 measurements from satellite, say 2000 onward, would be a more defensible choice. Given the
465 uncertainties associated with the AMSU-A window channel effects on the assimilation of
466 moisture, we believe this choice will remain ambiguous until specific satellite algorithm and bias
467 correction issues are studied more thoroughly with numerical experimentation.

468 **6. Results and Discussion**

469 *a. Adjusted time series for heat and water budget terms*

Figures 11 and 12 show area-averaged anomaly time series of the corrected budget quantities over separate global ocean and land domains. By construction the large trends in the original moisture and heating increments as well as precipitation and evaporation are now absent after applying the PCR procedure. These reductions are substantial over ocean but much smaller over land (compare to Figures 5 and 6). Perhaps the most notable result here is that, when averaged to global domains, the remaining increments are of the same size as the leading physical terms. Furthermore, whereas the unadjusted heating and moistening increments were also strongly correlated, they now have a much weaker relationship to each other. These remaining increments should be due largely to model physics inaccuracies interacting with time-varying flows, as well as remaining observational error. The latter may have both random and flow-dependent components. The moisture increments and evaporation are anti-correlated, as are the heating increments and dynamical heat transport. This is not surprising since we have removed the variability in these fluxes that correlates with the part of the increment signal induced by satellite sensor changes. But it also suggests that when moisture is added (or subtracted) by the increments to follow the observations, it acts to decrease (or increase) the near-surface humidity deficit and alter the evaporation accordingly. Likewise, if enthalpy increments constraining the analysis to temperature observations are positive, the dynamical response to this heating should be that heat is exported to land areas and potential energy lost to kinetic energy. The opposite argument holds for negative increments.

Bosilovich et al. (2010) noted significant changes in the increments, transports and fluxes over tropical continental regions between the decades before and since the availability of AMSU-A data. Because the changes in radiosonde moisture measurements in central Africa also

492 result in a local step-like change in a data stream they also project onto the low-frequency
493 variance of the leading increment and constitute a trend that gets removed.

494 Ideally, the next step would be to "explain" as much as possible of the remaining increments
495 in terms of statistical corrections to the model physics terms. This is the objective that Schubert
496 and Chang (1996) sought in their analysis of a much more limited data sample. We leave this
497 type adjustment for future work, but point out here the likely direction of such adjustments. Note
498 that the corrected moisture increment has some anti-correlation with ENSO signals, i.e., it is
499 subtracting (adding) moisture when SST is warm (cold), as does precipitation. If the moisture
500 increment is used entirely to adjust the precipitation rate (i.e. $P_q^* = - (MST_q + ANA_q)$, the
501 resulting global mean value agrees better with GPCP precipitation in terms of interannual
502 variability (Figure 13). There are some remaining departures in agreement between P_q^* and
503 GPCP such as in the mid 1990s, but here the agreement with the Hilburn and Wentz (2008)
504 SSMI precipitation over ocean (not shown) is better, underscoring the fact that significant
505 uncertainties remain with precipitation retrievals.

506 *b. Component Radiative Fluxes*

507 Another interesting aspect of the PCR adjustment is that, although the radiative heating term
508 in the atmospheric heat budget, RAD, has no large global trend in the raw MERRRA data this is
509 decidedly not so for the individual SW and LW fluxes at TOA and the surface. Significant
510 corrections through the PCR procedure are made to these component fluxes. Figure 14 shows
511 time series of these quantities before and after the correction. Except for OLR, significant step-
512 wise trends are present in each flux component. The strong correlation between TOA and
513 surface SW variations is present as expected (Ramanathan, 1986; Cess etal., 1991).

514 Selected non-ENSO EOFs of the unadjusted MERRA radiative flux components that
515 dominate their trend and annual cycle behavior are shown in Figure 15. The leading SW mode
516 corresponds to broadly increased precipitation-driven cloudiness over the warm pool region, the
517 eastern Pacific, and the Southern Ocean. Mode three of the TOA net SW captures a change in
518 annual cycle phase that maximizes at higher latitudes. The second OLR mode shows a decrease
519 with time consistent with increasing cloudiness over the warm pool. Surface LW increases are
520 ubiquitous over the global oceans and the PC of the leading mode correlates well with column
521 water vapor increases (not shown) suggesting that the onset of SSMI and eventually N15 and
522 N16 AMSU-A moisture data have a dominant impact on surface downward LW. It is notable
523 that the largest surface LW signal is present over central Africa where the decreasing moisture
524 convergence associated with the evolving rawinsonde signal in the unmodified MERRA data
525 projects strongly and indicates the effects of lower tropospheric drying.

526 The opposition of SW and LW fluxes and the significant correlation between SW at the
527 surface and TOA in Figures 13 and 14 have consequences for net atmospheric radiative cooling
528 and warming. The increase in water vapor increments with time sustains higher water vapor in
529 the lower troposphere which, in addition to enhancing downward LW at the surface, supports
530 more condensation and cloudiness. The subsequent SW reduction at the surface from the
531 increasing cloud fraction more than offset the increase in LW there and, in fact, results in the
532 decreasing net radiation to the surface of about 5 Wm^{-2}. High cold cloudiness associated with
533 increased tropical precipitation induced by increasing water vapor increments acts to reduce
534 OLR and offsets the increasing longwave loss to the surface. So, the net adjustments in SW and
535 LW brought about by the changing increments of water vapor (and temperature) are near-
536 canceling in terms of atmospheric radiative loss. But as in the case of surface changes, the

537 increased TOA SW cloud reflection overcomes the OLR signal to produce a net decrease of
538 about 5 Wm^{-2} in net radiation absorbed by the earth-atmosphere system which would be felt by
539 the ocean in a coupled system.

540 Adjustments derived from the PCR procedure are effective in identifying the step functions
541 in the fluxes related to the SSMI and AMSU-A data stream changes (Figures 11 and 12). Net
542 surface and TOA fluxes now have essentially no trend. Although the net effects of SW on the
543 atmosphere are small even before the correction, the spurious decrease in SWnet at the surface of
544 ~ 10 Wm^{-2} is removed by the PCR procedure. Of course the opposing LWnet trend of about half
545 that magnitude is also removed. In light of the mean 13.8 Wm^{-2} net energy flux bias to the ocean
546 in the 2000-2004 period noted by Bosilovich et al. (2010), the order 5 Wm^{-2} net ocean surface
547 radiative flux decrease over the 30-year MERRA period could mean significant biased forcing
548 for ocean and land models forced off line using these unadjusted fluxes. The signals associated
549 with ENSO events are now readily identifiable in the individual LW components with elevated
550 (suppressed) atmospheric LW cooling to space and to the surface during warm (cold) SST
551 events.

552 *c. Regional decadal signals*

553

554 With the removal of global mean trends from the fluxes there is concern that any long term
555 climate signals may also have been removed. The statistical nature of the PCR procedure is
556 incapable of distinguishing a physical trend in the fluxes from that induced by one or more step-
557 like artifacts in the increments. However, this does not necessarily mean that regional trends or
558 variability that does not project on a near-global domain is removed. Here, we re-examine the
559 PDV signal in MERRA to see how the PCR adjustment has affected the realism of this feature.

560 Figure 16 shows the regression of original and corrected precipitation, evaporation, and TOA net
561 SW flux onto the PC. There are striking differences between the adjusted and original quantities.
562 In the adjusted data, there is a distinct decrease in precipitation over the equatorial western
563 Pacific and increases in the eastern equatorial Pacific and over the western Pacific subtropics
564 which agree well with the result using GPCP precipitation (Figure 10) and with the results of
565 Burgman et al., (2008) who used SSMI retrievals from Remote Sensing Systems (Hilburn and
566 Wentz, 2008). These features are distorted in the unadjusted MERRA data. The net radiative
567 heating, RAD, responds to cloudiness changes and mirrors the effects of the PCR adjustments
568 over the western Pacific, but it also indicates the substantially different response in the
569 cloudiness in the eastern Pacific. The unadjusted evaporation pattern is essentially the same as
570 that for its leading EOF (not shown) whereas after the correction much of the same structure
571 remains, but with smaller amplitude.

572 Because the PDV SST signal used in the regression is to first order a trend, any other signal
573 having a trend will be picked up to some extent, whether or not it is physically related to the
574 PDV mechanism. We see that in central Africa, the downward trend in precipitation and
575 evaporation that is likely erroneous (Bosilovich et al., 2010) has also been greatly reduced. This
576 has occurred because of the temporal coherence between the analysis increment, ANA_q, and the
577 physical budget terms which oppose the increment as noted in section 4b. It is perhaps fortuitous
578 that AMSU-A timing of data availability and the change in rawinsonde instrumentation both
579 induce low frequency trends components of opposite sign.

580 Clearly the PCR procedure has resulted in significant differences. Based on the better
581 precipitation comparisons, it appears that the PCR adjustments enable a much clearer picture of

582 the low frequency behavior of fluxes during the MERRA period. More analysis is needed to
583 confirm the degree to which this is so.

584 ## *7.* Conclusions

585 Like all reanalysis efforts MERRA has to contend with an inhomogeneous observing
586 network. From a climate perspective, the satellite era (~ 1979 onward) arguably presents the
587 largest challenges to assimilation efforts because of the significant but discreet advances in
588 remote sensing of water vapor and clouds. Here we have addressed the two most obvious
589 observing systems epoch changes, the AMSU-A series in late 1998 and, to a lesser extent, the
590 earlier advent of SSMI in late 1987. More specifically, the window channels of AMSU-A have
591 been found to produce a strong influence on MERRA water vapor increments that changes their
592 global mean sign from negative to positive. By virtue of the moisture increment influence on net
593 condensation (precipitation), the heating increment anomalies turn negative. The total increment
594 of heating (climatological mean plus anomaly) thus falls to its smallest positive magnitude
595 during the post-1979 period. The dominant pattern of variability for the moisture increment is the
596 stepwise increase in moisture over the tropical oceans, particularly the warm pool and inter-
597 American Seas during NH Summer. Drying of the Southern Ocean region during the tenure of
598 SSMI is reversed with the onset of AMSU-A data. As tropical ocean precipitation increases in
599 response to this additional moisture, the heating increment anomalies change from warming to
600 cooling over the western Pacific and much of the Indian Ocean while remaining positive over
601 land areas.

602 We also find that aspects of the annual cycle are affected by the sensor changes. Removing a
603 mean annual cycle defined over the entire period leaves signals in the fluxes that still have power

604 at the annual time scale, indicating that a non-stationary the annual cycle has been induced by the
605 satellite changes. This leads to the question of what period should be regarded as the one over
606 which the climatological mean is defined. One would logically expect the most recent era from
607 2000 onwards as having the most accurate data with which to constrain the GEOS-5 model. But
608 this choice carries the implicit assumption that the degrading effects of possible biases in the
609 algorithm, instrument, or forward radiative transfer modeling are outweighed by the increased
610 ability of the augmented observations to correct model physics- induced biases. We do not
611 believe this issue is settled, and we are currently analyzing diagnostics of the bias corrections to
612 understand more fully the origin of the increased moisture increments from SSMI to AMSU-A.

613 EOF analysis reveals that the increment artifacts are largely captured by approximately five
614 modes (the first four plus the seventh in the case of the moisture budget, and the leading five for
615 the heat budget). Principal Component Regression was found useful in isolating and greatly
616 reducing artifacts produced by changes of satellite sensors. The method uses the patterns of
617 variability contained within a subset of increment modes that capture the discontinuities in
618 increment forcing to predict a corresponding sequence of modes in each of the flux terms. We
619 have shown that after the adjustments are applied, the spurious trend components related to the
620 assimilationt of the SSMI and AMSU data are largely eliminated. Although the net radiative
621 heating term in the enthalpy budget does not have nearly the trend amplitude compared to the
622 precipitation term (or the forcing ANA_H), the TOA and surface net SW and the surface net LW
623 components do. The adjustment process is effective in removing these spurious signals. Perhaps
624 the most encouraging evidence for the utility of this approach is present in Figure 13 where the
625 corrected global mean precipitation anomalies were found to relate well to the variability in
626 GPCP precipitation. This also means that, to the extent of our confidence in global mean GPCP

627 values, the global area averaged time series of evaporation estimates recovered from the
628 corrected MERRA are also more accurate. It was also shown that simply using the raw
629 assimilated fields from MERRA to diagnose Pacific Decadal Variability leads to distorted
630 signals. The patterns of precipitation covariance with the PDV SST mode obtained from the
631 adjusted data were in much better agreement with recent diagnostics (Burgman et al., 2008)
632 using independent satellite precipitation measurements from SSMI (Hilburn and Wentz, 2008).

633 The PCR technique (and ultimately, any linear regression method) is not without problems as
634 it is not possible to distinguish between trends associated with physical processes and those
635 arising as a consequence of the step functions. The selection of those increment modes deemed
636 to be associated with the satellite-induced artifacts is ultimately a subjective process. As is
637 frequently the case, individual EOFs and their PCs cannot usually be equated purely with
638 physical modes. Here too we cannot expect individual events where sensors change to be
639 captured by a single mode of the increments. Instead it takes several modes to effectively
640 describe the collective effects of the sensor changes. One might consider alternative strategies
641 such as a regression of the fluxes on SST to recover the physical variability associated with
642 climate variations. In the case of ENSO, this is possible since the leading mode has very little
643 trend. In contrast, signals such as that of the PDV which dominates the global SST trend would
644 end up retaining also the non-physical trends induced by stepwise increment changes. While we
645 have not attempted to quantify the error associated with the PCR procedure, *a posteriori*
646 comparisons to independent observational data may provide the best assessment of how sensitive
647 the results are to the selection of predictor modes.

648 It is anticipated that the analysis of the MERRA fluxes and the statistical adjustments
649 presented here will add to the utility of the MERRA data set in climate diagnostics studies.

650 Many types of studies using MERRA data should be largely immune to the problems of time
651 dependent bias. These would include, for example, compositing studies, various diagnostics on
652 processes at the synoptic to intraseasonal scale, or any study in which the characteristic time
653 scale is short compared to time intervals between significant sensor changes. For studies of
654 variability on interannual and longer time scale, the issues presented here should be considered
655 when interpreting the results. The degree to which our statistical adjustments can be taken a step
656 further to partition the remaining systematic increment variability among the physical budget
657 terms is currently under study. The approach of Schubert and Chang (1996) provides one
658 potential methodology. But whether the assumptions made in that study which used 6h data over
659 a limited region for several months can be extended to global, monthly data sets is unknown.

660 An important complement to the adjustment strategy analysis presented here involves the use
661 of multiple data withholding experiments to determine the contribution of each observing system
662 change to the evolving time series of fluxes. This avenue is actively being pursued. Ultimately
663 the answer to the problem of uncertainties induced via observing system changes lies both in
664 reducing model errors, in more robust bias correction strategies and in more mature
665 understanding of sensor retrieval algorithms that will be employed in future reanalysis efforts.
666 These are ongoing challenges being addressedt at all institutions involved in data assimilation
667 activities.

668 *Acknowledgements.* This study was supported by the NASA Energy and Water Cycle
669 Study (NEWS) and by NASA Modeling Analysis and Prediction Program (MAP). The authors
670 thank Dr. Emily Liu, GSFC for producing the MERRA withholding experiments and for
671 discussion of these results. Also, Drs. Max Suarez and Siegfried Schubert provided many

672 thoughtful comments and discussions concerning results in this paper. We are especially grateful
673 to Dr. Ron Gelaro whose comments substantially improved an earlier version of this paper.
674
675
676

677 **8. References**

678 Adler, R.F., and Coauthors, 2003: The Version-2 Global Precipitation Climatology Project
679 (GPCP) monthly precipitation analysis (1979–Present). *J. Hydrometeor*, **4**, 1147–1167.

680 Andersson, E., P. Bauer, A. Beljaars, F. Chevallier, E. Hólm, M. Janisková, P. Kållberg, G.
681 Kelly, P. Lopez, A. Mcnally, E. Moreau, A.J. Simmons, J.N. Thépaut, and A.M.
682 Tompkins, 2005: Assimilation and Modeling of the Atmospheric Hydrological Cycle in
683 the ECMWF Forecasting System. *Bull. Amer. Meteor. Soc.*, **86**, 387–402.

684 Bakalian, F. H. Ritchie, K. Thompson, and W. Merryfield, 2010: Exploring Atmosphere–Ocean
685 Coupling Using Principal Component and Redundancy Analysis, *J. Climate*, **23**, 4926-4943,
686 doi: 10.1175/2010JCLI3388.1.

687 Berrisford, P., D. P. Dee, K. Fielding, M. Fuentes, P. Kallberg, S. Kobayashi, and S. Uppala
688 2009. 'The ERA-Interim Archive'. *ERA Report Series* No. 1, ECMWF: Reading, UK
689 (available from www.ecmwf.int/publications).

690 Bloom, S. C., L. L. Takacs, A. M. da Silva, and D. Ledvina, 1996: Data assimilation using
691 incremental analysis updates. *Mon. Wea. Rev.*, **124**, 1256–1271.

692 Bosilovich, M.G., F.R. Robertson and J. Chen, 2010: Global energy and water budgets in
693 MERRA (*J. Climate*, submitted).

694 Bove, M. C., J. J. O'Brien, J. B. Eisner, C. W. Landsea, and X. Niu, 1998: Effect of El Niño on
695 U.S. landfalling hurricanes, revisited. *Bull. Amer. Meteor. Soc.*, **79**, 2477-2482.

696 Burgman, R. J., A. C. Clement, C. M. Mitas, J. Chen, and K. Esslinger, 2008: Evidence for
697 atmospheric variability over the Pacific on decadal timescales, *Geophys. Res. Lett.*, *35*,
698 L01704, doi:10.1029/2007GL031830.

699 Chen, J., A.D. Del Genio, B.E. Carlson, and M.G. Bosilovich, 2008: The spatiotemporal
700 structure of twentieth-century climate variations in observations and reanalyses. Part I: Long-
701 term trend. *J. Climate*, **21**, 2611-2633, doi:10.1175/2007JCLI2011.1.

702 Chen, J., A.D. Del Genio, B.E. Carlson, and M.G. Bosilovich, 2008: The spatiotemporal
703 structure of twentieth-century climate variations in observations and reanalyses. Part II:
704 Pacific pan-decadal variability. *J. Climate*, **21**, 2634-2650, doi:10.1175/2007JCLI2012.1.

705 Cess, R. D., E. G. Dutton, J. J. DeLuisi, and F. Jiang, 1991: Determining surface solar absorption
706 from broadband satellite measurements for clear skies: Comparison with surface
707 measurements. *J. Climate,* **4,** 236–247.

708 Curtis, S. and R. Adler, 2000: ENSO Indices Based on Patterns of Satellite-Derived
709 Precipitation. *J. Climate*, **13**, 2786–2793. doi: 10.1175/1520-0442(2000)013.
710 Dee, D.P. 2004: 'Variational bias correction of radiance data in the ECMWF system'. In
711 *Proceedings of workshop on assimilation of high spectral resolution sounders in NWP,*
712 *Reading, UK, 28 June–1July 2004*. ECMWF: Reading, UK. pp 97–112.
713 Dee, D.P. 2005: Bias and data assimilation. *Q. J. R. Meteorol. Soc.* **131**:3323–3343.
714 Dee, D. P. and R. Todling, 2000: Data assimilation in the presence of forecast bias: The GEOS
715 moisture analysis. *Mon. Wea. Rev.*, **128**:3268–3282.
716 Dee, D.P. and S. Uppala, 2008: Variational bias correction of satellite radiance data in theERA-
717 Interim reanalysis *Q. J. R. Meteorol. Soc.* **135**: 1830–1841 (2009) DOI: 10.1002/qj.493.
718 Derber, J.C, and W.-S. Wu, 1998: The use of TOVS cloud-cleared radiances in the NCEP SSI
719 analysis system. *Mon. Weather Rev.* **126**: 2287–2299.

720 Deser, C., A. S. Phillips, and J. W. Hurrell, 2004: Pacific interdecadal climate variability:
721 Linkages between the Tropics and North Pacific during boreal winter since 1900. *J. Climate,*
722 **17,** 3109–3124.
723 Dole, R. M., 1989: Life cycles of persistent anomalies. Part 1: Evolution of 500mb height
724 anomalies. *Mon. Wea. Rev*., **117**, 177-211.
725 Enfield, D. B., A. M. Mestas-Nun˜ez, and P. J. Trimble (2001), The Atlantic Multidecadal
726 Oscillation and its relation to rainfall and river flows in the continental U.S., *Geophys. Res.*
727 *Lett.*, **28**, 2077– 2080.
728 Gill, A.E., 1980: Some simple solutions for heat-induced tropical circulations. *Quart. J. Royal*
729 *Meteor. Soc.*, **106**, 447-462
730 Gu, G., R. F. Adler, G. J. Huffman, and S. Curtis, 2007: Tropical Rainfall Variability on
731 Interannual-to-Interdecadal and Longer Time Scales Derived from the GPCP Monthly
732 Product. *J. Climate*., **20**, 4033-4046 doi: 10.1175/JCLI4227.1.
733 Han, Y., P. van Delst, Q. Liu, F. Weng, B. Yan, R. Treadon, and J. Derber, 2006: JCSDA
734 Community Radiative Transfer Model (CRTM) - Version 1. NOAA Tech. Rep.NESDIS 122,
735 33 pp.
736 Harris, B.A., and G.A. Kelly, 200: A satellite radiance bias correction scheme for data
737 assimilation. *Quart. J. Roy. Meteor. Soc*., **127**, 1453–1468.
738 Hilburn, K. A. and F. J. Wentz, 2008: Intercalibrated passive microwave rain products from the
739 unified microwave ocean retrieval algorithm (UMORA), *J. Appl. Meteor. and Clim.*, **47**, 778-
740 794.
741 Hoskins, B.J. and D.J. Karoly, 1981: The steady linear response of a spherical atmosphere to
742 thermal and orographic forcing, *J. Atmos. Sci*., **38**, 1179-1196,

743 Hoskins, B. J., K. I. Hodges, 2005: A New Perspective on Southern Hemisphere Storm Tracks. *J.*
744 *Climate*, **18**, 4108-4129.
745 Okamoto, K. and J. C. Derber, 2006: Assimilation of SSM/I Radiances in the NCEP Global
746 Data Assimilation System, *Mon. Wea. Rev.,* **134**:9, 2612-2631.
747 Onogi, K., and Coauthors, 2007: The JRA-25 reanalysis. *J. Meteor. Soc. Japan,* **85,** 369–432.
748 Ramanathan, V., 1986: Scientific use of surface radiation budget for climate studies. Surface
749 Radiation Budget for Climate Applications. NASA RP-1169, 58–86.
750 Rienecker, M.M., M.J. Suarez, R. Todling, J. Bacmeister, L. Takacs, H.-C. Liu, W. Gu, M. 638
751 Sienkiewicz, R.D. Koster, R. Gelaro, I. Stajner, and E. Nielsen, 2009: *The GEOS-5 Data* 639
752 *Assimilation System- Documentation of Versions 5.0.1, 5.1.0, and 5.2.0*. Technical Report
753 640 Series on Global Modeling and Data Assimilation, NASA/TM-2007-104606, M.J.
754 Suarez, 641 Ed., Vol. 27, 95 pp. 642.
755 Rienecker M.M., and coauthors, 2010. The NASA Modern Era Retrospective-Analysis for 643
756 Research and Applications (MERRA). *J. Climate* (in preparation).
757 Ropelewski, C. F. and M. S. Halpert, 1987: Global and regional scale precipitation patterns
758 associated with the El Niño/Southern Oscillation cycle. *Mon. Wea. Rev*., **115**, 1606-1626.
759 Schubert and Chang, 1996
760 Schlesinger, M. E., and N. Ramankutty, An oscillation in the global climate system of period 65-
761 70 years, *Nature*, **367**, 723-726, 1994.
762 Simmonds, I., and K. Keay, 2000: Mean Southern Hemisphere extratropical cyclone behavior in
763 the 40-Year NCEP–NCAR Reanalysis. *J. Climate*, **13**, 873-885
764 Sterl, A., 2004: On the (In)Homogeneity of reanalysis products. *J. Climate*, **17**, 3866-3873.

765 Suarez, M. and co-authors, 2010: File Specification for MERRA Products. Global Modeling and
766 Assimilation Office, Greenbelt MD.
767 [http://gmao.gsfc.nasa.gov/research/merra/file_specifications.php]
768 Thompson, David W. J., John M. Wallace, 2000: Annular modes in the extratropical circulation.
769 Part I: month-to-month variability. *J. Climate*, **13**, 1000-1016.
770 Thompson, David W. J., John M. Wallace, Gabriele C. Hegerl, 2000: Annular modes in the
771 extratropical circulation. Part II: Trends. *J. Climate*, **13**, 1018-1036.
772 Thompson, D. W. J, and J. M. Wallace, 1998: The Arctic Oscillation signature in the wintertime
773 geopotential height and temperature fields. *Geophys. Res. Lett.,* **25,** 1297–1300.
774 Trenberth, K. E., T. Koike, and K. Onogi, 2008: Progress and prospects in reanalysis. *Eos*, **89**,
775 26, 24 June 2008, 234-235.
776 Trenberth, K.E., J.T. Fasullo, and J. Kiehl, 2009: Earth's Global Energy Budget. *Bull. Amer.*
777 *Meteor. Soc.*, **90**, 311–323.
778 Trenberth, K. E., D. P. Stepaniak, J. W. Hurrell and M. Fiorino, 2001: Quality of reanalyses in
779 the tropics. *J. Climate*, **14**, 1499-1510.
780 Trenberth, K. E., D. P. Stepaniak and J. M. Caron, 2000: The global monsoon as seen through
781 the divergent atmospheric circulation. *J. Climate*, **13**, 3969-3993.
782 Trigo, R. M., I. F. Trigo, C. C. DaCamara, and T. J. Osborn, 2004: Climate impact of the
783 European winter blocking episodes from the NCEP/NCAR Reanalyses., *Climate Dynamics*,
784 **23**, 17–28, DOI 10.1007/s00382-004-0410-4.
785 von Storch, H., and F. Zwiers, 1999: Statistical Analysis in Climate Research. Cambridge
786 University Press, 484 pp.

787 Zhang, Y., J. M. Wallace, and D.S. Battisti, 1997: ENSO-like interdecadal variability: 1900–93.
788 *J. Climate*, **10**, 1004–1020.
789 Wang, C., 2002: Atmospheric Circulation Cells Associated with the El Niño–Southern
790 Oscillation. *J. Climate*, **15**, 399-419.
791 Wang, X., and F. Zwiers, 2001: Using redundancy analysis to improve dynamical seasonal mean
792 500-hPa geopotential forecasts. *Int. J. Climatol*., **21**, 637–654.
793

Figure Captions

Figure 1. Time mean (1979-2007) MERRA vertically integrated moisture (mm day^{-1}) and heating increments (W m^{-2}).

Figure 2. Zonal mean anomalies of moisture (mm day^{-1}) and heating (W m^{-2}) increments. Anomalies are departures from climatological mean seasonal cycle. Onset times of data availability for the SSMI and AMSU-A sensors are Aug1987 and Nov1998, respectively.

Figure 3. Top: Analysis minus forecast NOAA15 AMSU-A CH15 (89 GHz, window channel) brightness temperatures (K) averaged over the period Jan1999 through Dec2002. Bottom: Same except for CH5 (53.6 GHz, lower-tropospheric channel).

Figure 4. Global mean precipitation time series from MERRA and two data withholding experiments starting 02 Nov 1998. Experiment m98a withholds AMSU-A window channels (Ch 1, 2, 3 and 15) from the assimilation. Experiment m98b keeps those channels but applies no cloud liquid water bias correction to them.

Figure 5. Global ocean and land area-average moisture budget anomalies (mm day^{-1}). Moist processes ≅ precipitation (green), evaporation (cyan), vertically-integrated moisture flux convergence (red) and moisture increment (black). Anomalies are departures from monthly mean climatological mean values over the 1979-2009 period which are noted in their appropriate color. Shaded curve is Nino 3.4 SST anomaly x 0.10.

Figure 6. Same as Fig. 5 except for the virtual enthalpy budget with units Wm^{-2}. Time series of heating anomalies by moist processes (green), dynamics (red), radiative processes (blue), dynamical processes (red), turbulence or sensible heat flux (cyan), and analysis increment (black) are plotted with the climatological mean values also shown in their respective colors. Shaded curve is Nino 3.4 SST anomaly x 5.0.

Figure 7. EOFs and principal components (PCs) for modes 1-4 and 7 of the vertically-integrated moisture increment, ANA_q. Fractional variance explained refers to departures from the monthly varying annual mean defined by the period 1979-2009. EOFs carry the units of mm d^{-1} and scaling is such that the product of a PC and its EOF recover the contribution of that mode to the total increment anomaly.

Figure 8. Same as figure 7 except for modes 1-5 of the enthalpy increment ANA_H. Units of the EOFs are W m^{-2}.

Figure 9. Regression slopes for flux terms in moisture budget (left column, units mm d^{-1}) and enthalpy budget (right column, units W m^{-2}) against the global skin temperature anomalies (T_s, top left) filtered to retain only ENSO-related signals. Slopes are normalized to the SD (0.062 K) of the T_s time series. Values in parentheses are global means per SD.

Figure 10. The leading SST PC (normalized) and EOF after the global ENSO signals have been removed. Original MERRA and GPCP precipitation regressed against PC1 with units of mm d^{-1}. See text for details on the methodology.

Figure 11. Global ocean and land area-average moisture budget anomalies (mm day^{-1}) after PCR removal of artifact signals. Budget terms are: Moist processes ≅ precipitation (green), evaporation (cyan), vertically-integrated moisture flux convergence (red) and moisture increment (black). Anomalies are departures from monthly mean climatological mean values over the 1979-2009 period which are also noted in their appropriate color. Shaded curve is Nino 3.4 SST anomaly x 0.05.

Figure 12. Same as Figure 11 but for enthalpy budget. Units are W m^{-2}. Time series of heating anomalies by moist processes (green), dynamics (red), radiative processes (blue), dynamical processes (red), turbulence or sensible heat flux (cyan), and analysis increment (black) are plotted with the climatological mean values also shown in their respective colors. Shaded curve is Nino 3.4 SST anomaly x 1.5 (over ocean) and x 5.0 (over land).

Figure 13. The quantity $P_q^* \equiv -1.0 \times (MST_q + ANA_q)$ averaged over the globe +/- 60^o (black) compared to GPCP precipitation (dotted). Units are mm d^{-1}.

Figure 14. Radiative flux components (Wm^{-2}): original (dashed) and corrected (solid). Top: Surface net LW (black) and net SW(red). Middle: TOA OLR (black) and net SW (red). Bottom: Net atmospheric cooling by LW (black) and SW (red).

Figure 15. Selected EOFs and PCs from analysis of individual component fluxes. PCs are normalized so that EOFs carry the units of Wm^{-2}.

Figure 16. Adjusted and original regression maps of MERRA fluxes on the PC in Figure 9: (Top) precipitation, mm d^{-1}; (Middle) evaporation, mm d^{-1}; (Bottom) net atmospheric radiative heating, Wm^{-2}.

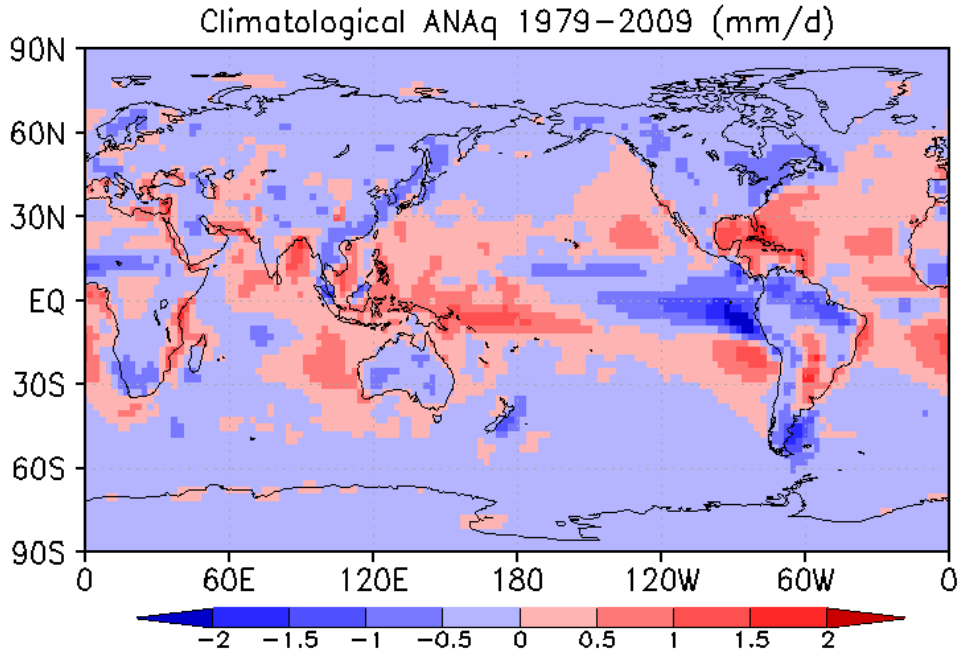

858

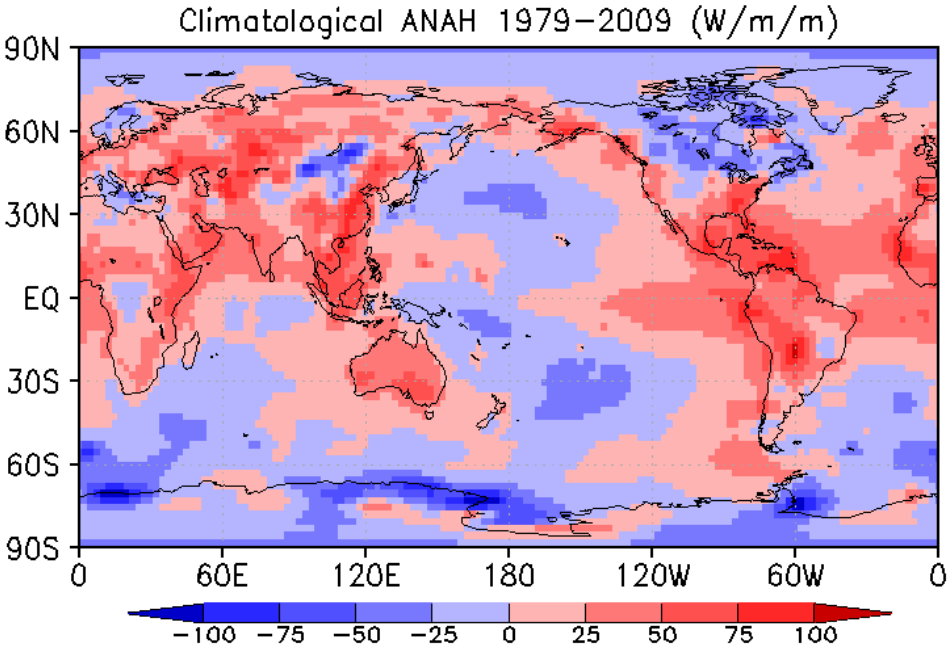

859
860

861 Figure 1. Time mean (1979-2007) MERRA vertically integrated moisture (mm day^{-1}) and
862 heating increments (W m^{-2}).

863

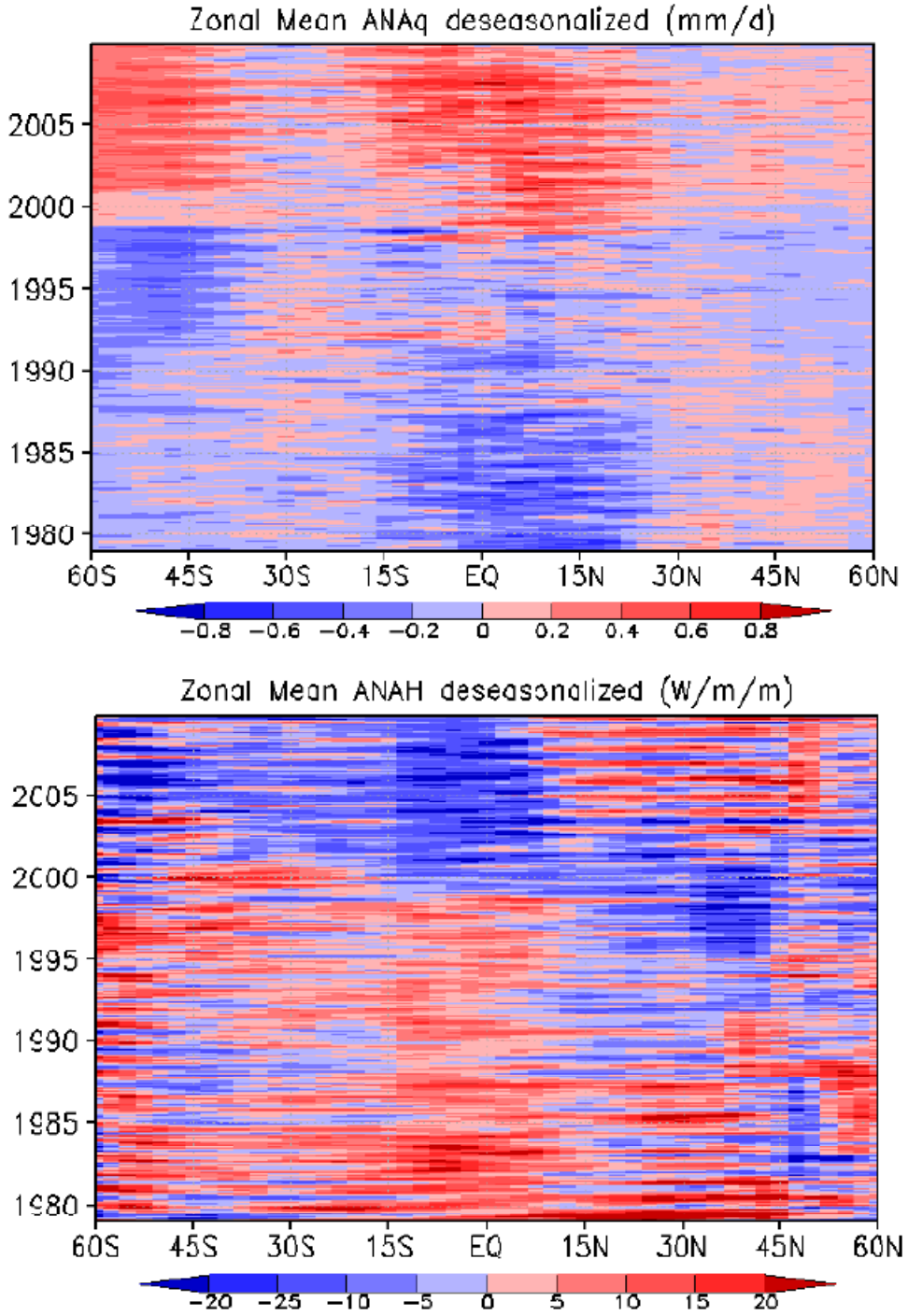

Figure 2. Zonal mean anomalies of moisture (mm day^{-1}) and heating (W m^{-2}) increments. Anomalies are departures from climatological mean seasonal cycle. Onset times of data availability for the SSMI and AMSU-A sensors are Aug1987 and Nov1998, respectively.

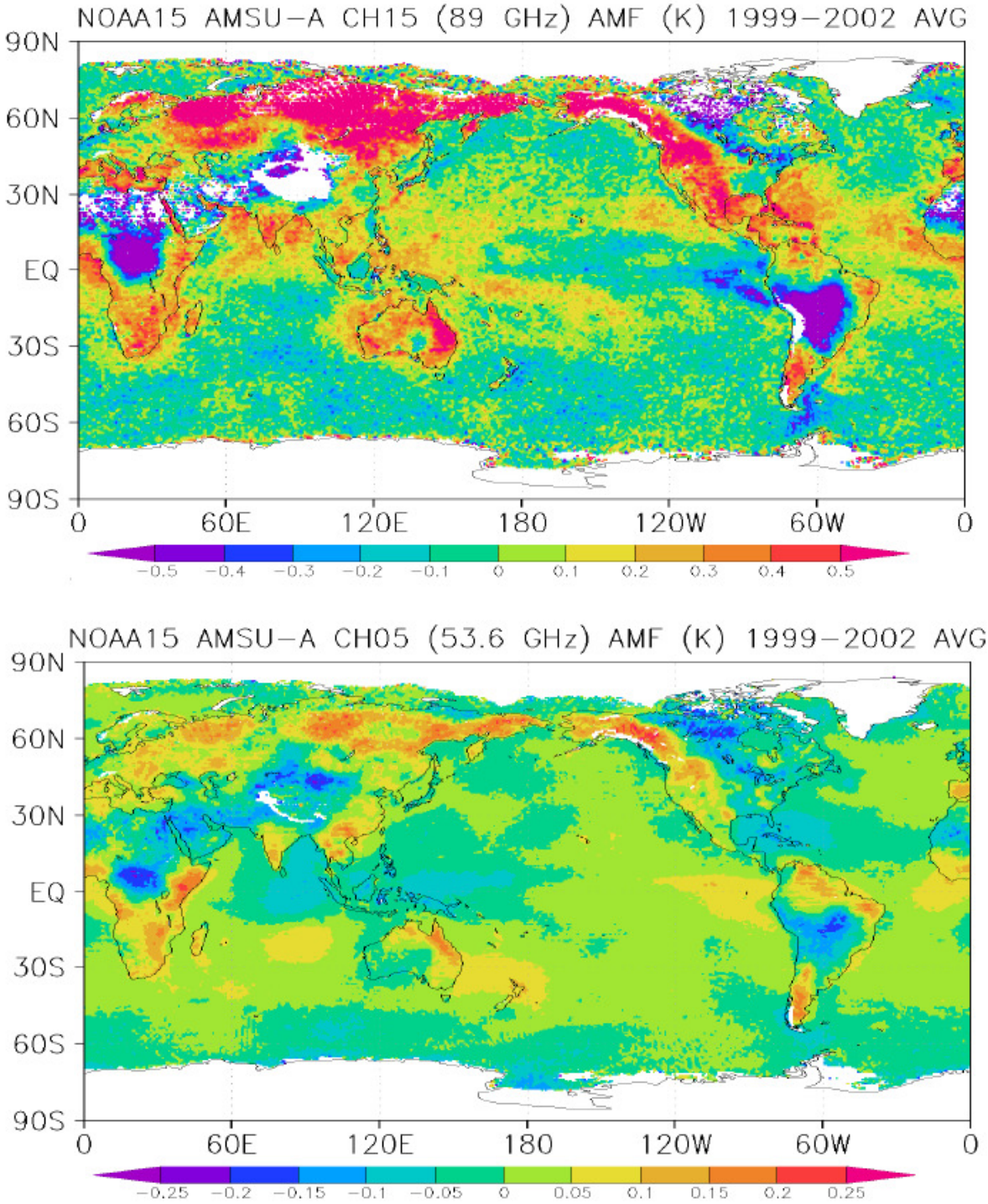

Figure 3. Top: Analysis minus forecast NOAA15 AMSU-A CH15 (89 GHz, window channel) brightness temperatures (K) averaged over the period Jan1999 through Dec2002. Bottom: Same except for CH5 (53.6 GHz, lower-tropospheric channel).

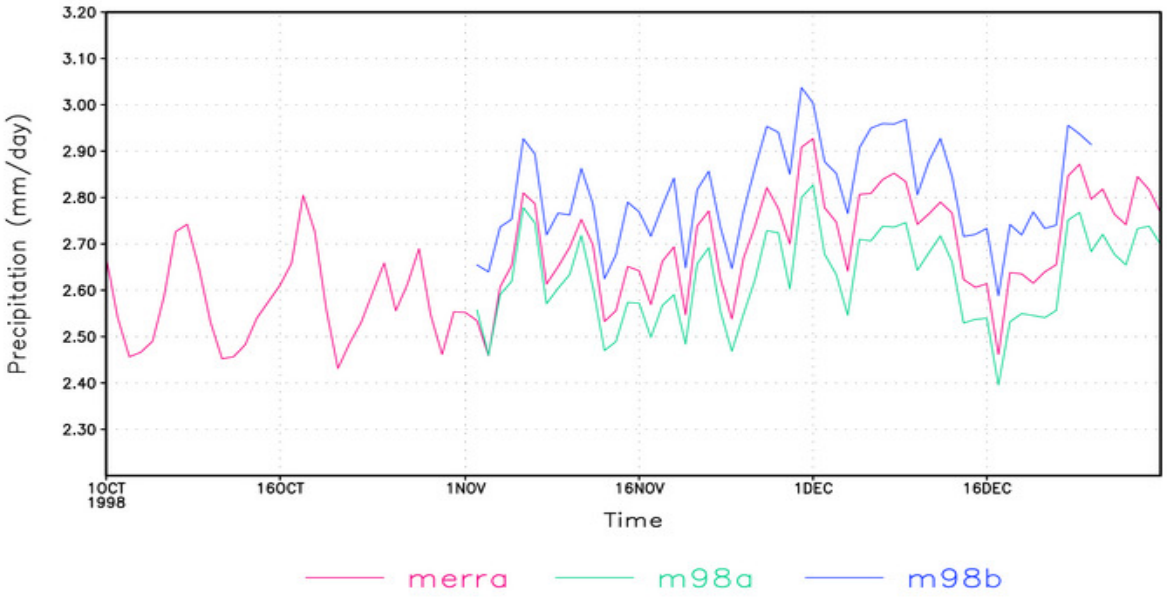

Figure 4. Global mean precipitation time series from MERRA and two data withholding experiments starting 02 Nov 1998. Experiment m98a withholds AMSU-A window channels (Ch 1, 2, 3 and 15) from the assimilation. Experiment m98b keeps those channels but applies no cloud liquid water bias correction to them.

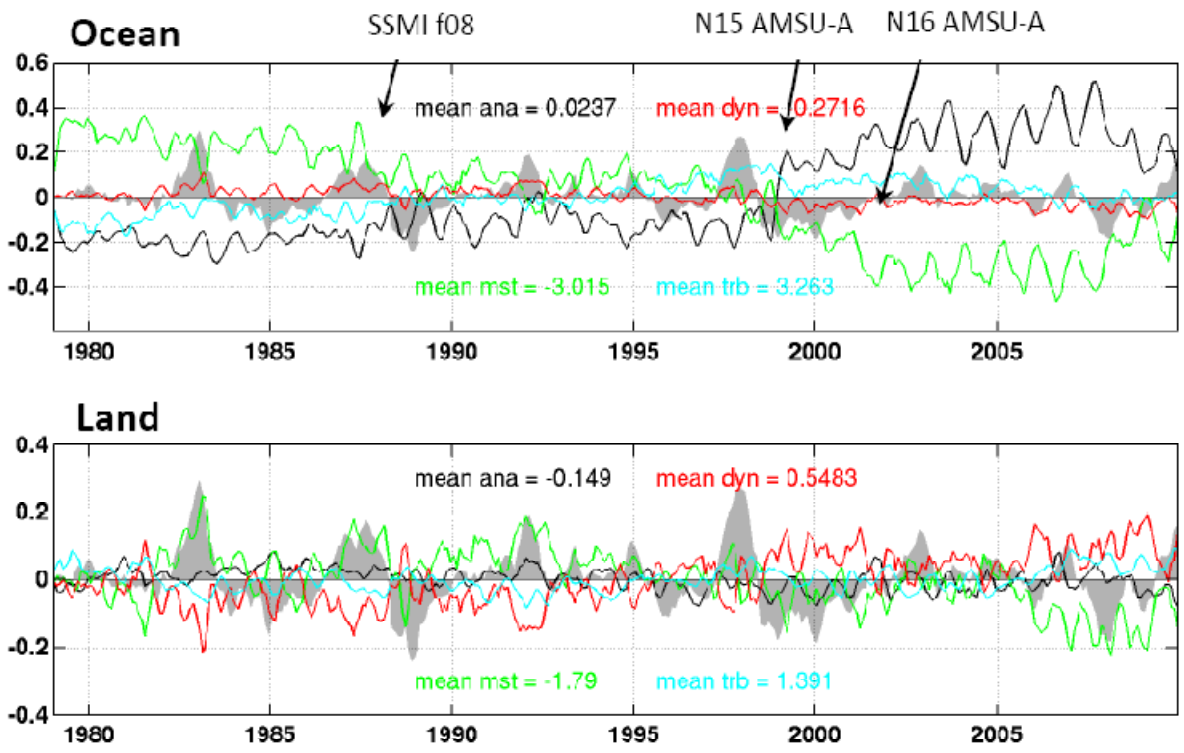

Figure 5. Global ocean and land area-average moisture budget anomalies (mm day^{-1}). Moist processes ≅ precipitation (green), evaporation (cyan), vertically-integrated moisture flux convergence (red) and moisture increment (black). Anomalies are departures from monthly mean climatological mean values over the 1979-2009 period which are noted in their appropriate color. Shaded curve is Nino 3.4 SST anomaly x 0.10.

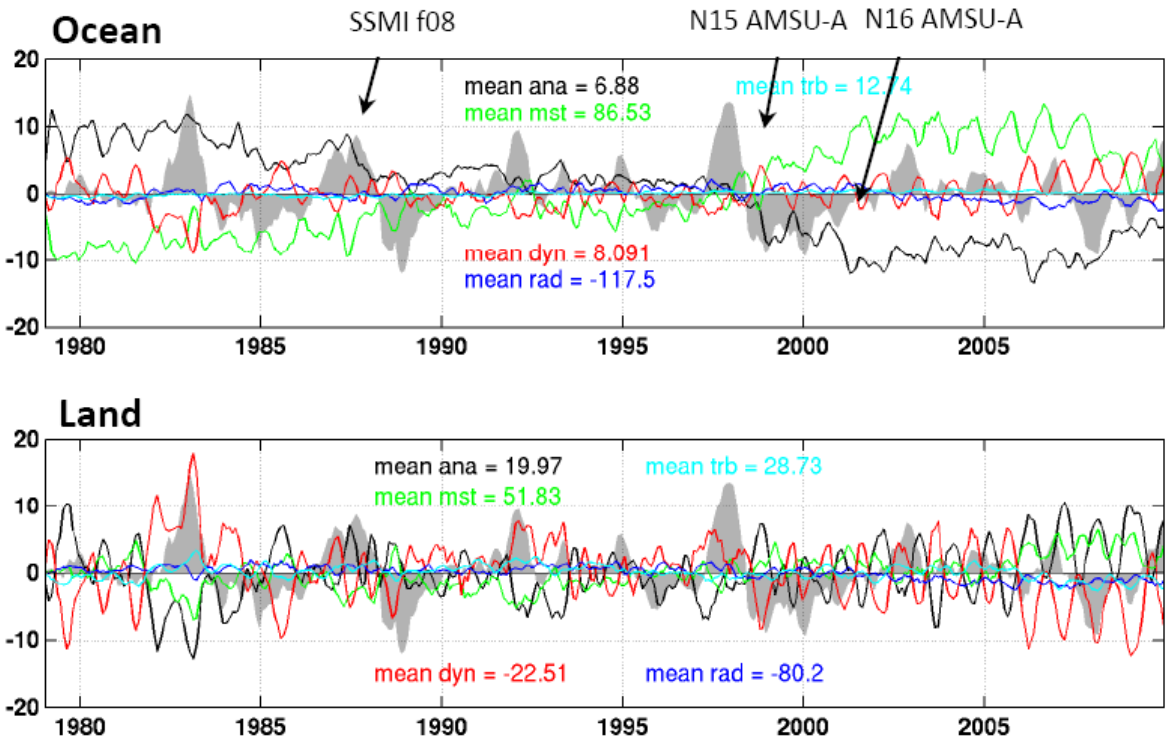

Figure 6. Same as Fig. 5 except for the virtual enthalpy budget with units Wm^{-2}. Time series of heating anomalies by moist processes (green), dynamics (red), radiative processes (blue), dynamical processes (red), turbulence or sensible heat flux (cyan), and analysis increment (black) are plotted with the climatological mean values also shown in their respective colors. Shaded curve is Nino 3.4 SST anomaly x 5.0.

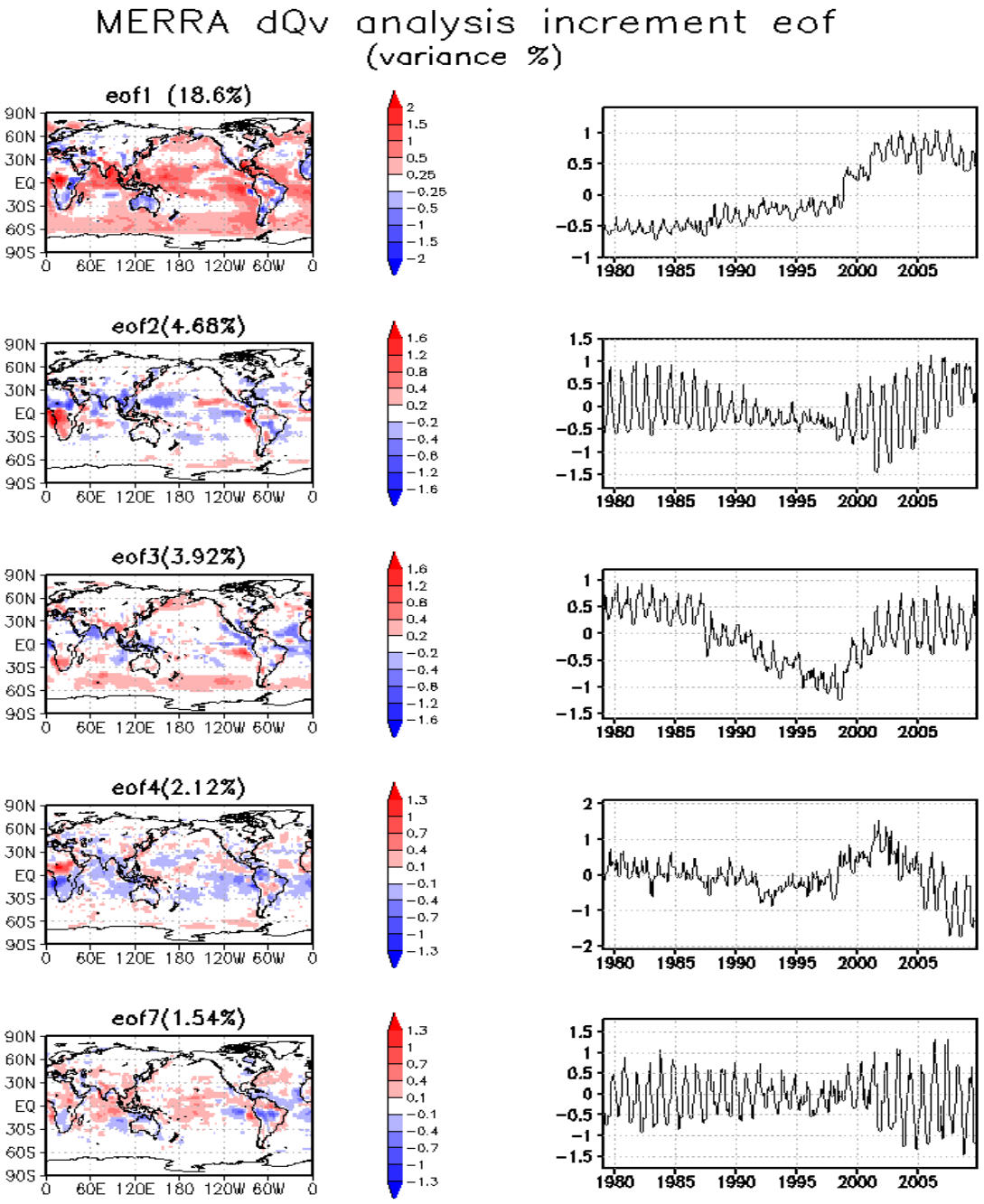

Figure 7. EOFs and principal components (PCs) for modes 1-4 and 7 of the vertically-integrated moisture increment, ANA_q. Fractional variance explained refers to departures from the monthly varying annual mean defined by the period 1979-2009. EOFs carry the units of mm d^{-1} and scaling is such that the product of a PC and its EOF recover the contribution of that mode to the total increment anomaly.

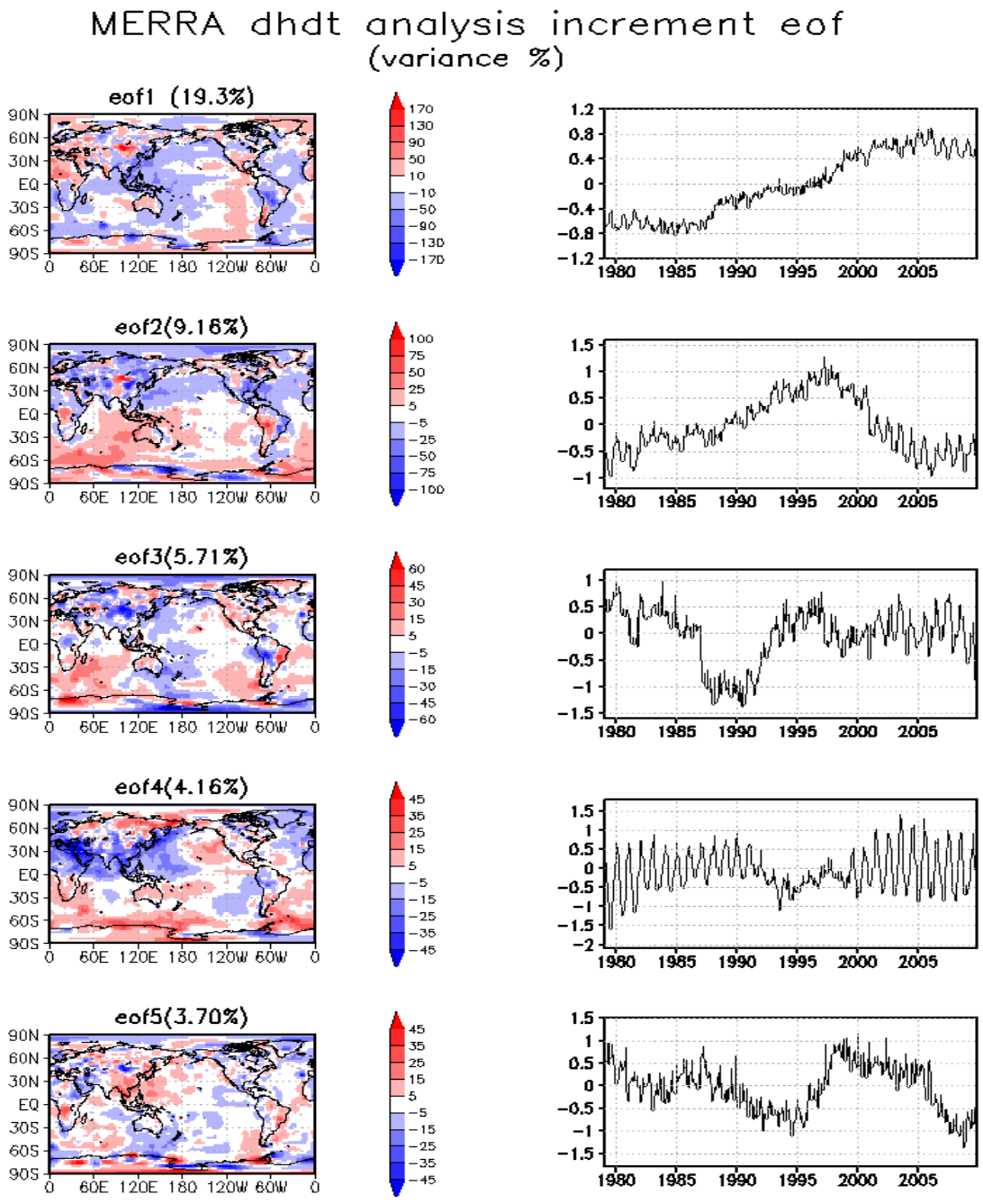

Figure 8. Same as figure 7 except for modes 1-5 of the enthalpy increment ANA_H. Units of the EOFs are W m^{-2}.

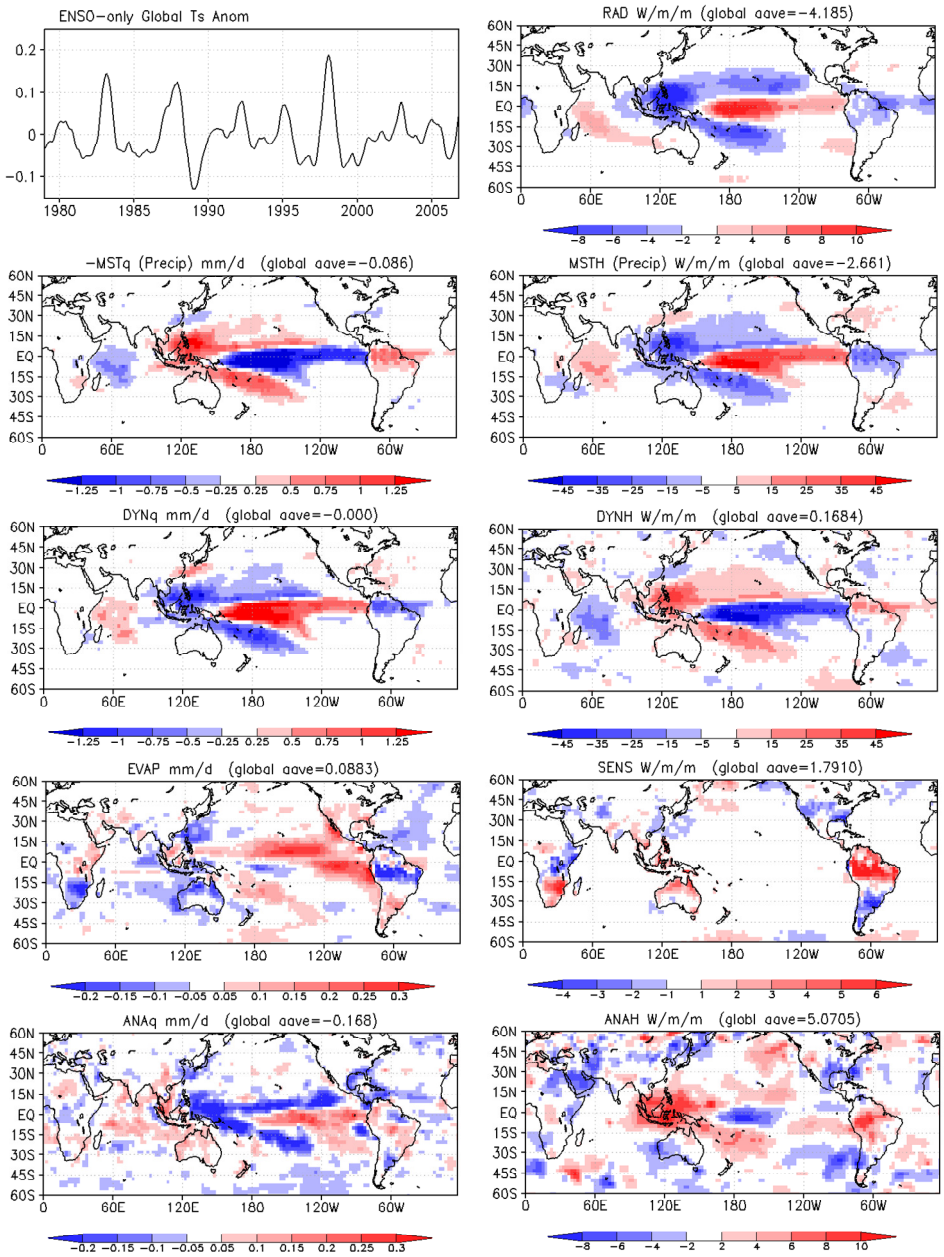

Figure 9. Regression slopes for flux terms in moisture budget (left column, units mm d^{-1}) and enthalpy budget (right column, units W m^{-2}) against the global skin temperature anomalies (T_s, top left) filtered to retain only ENSO-related signals. Slopes are normalized to the SD (0.062 K) of the T_s time series. Values in parentheses are global means per SD.

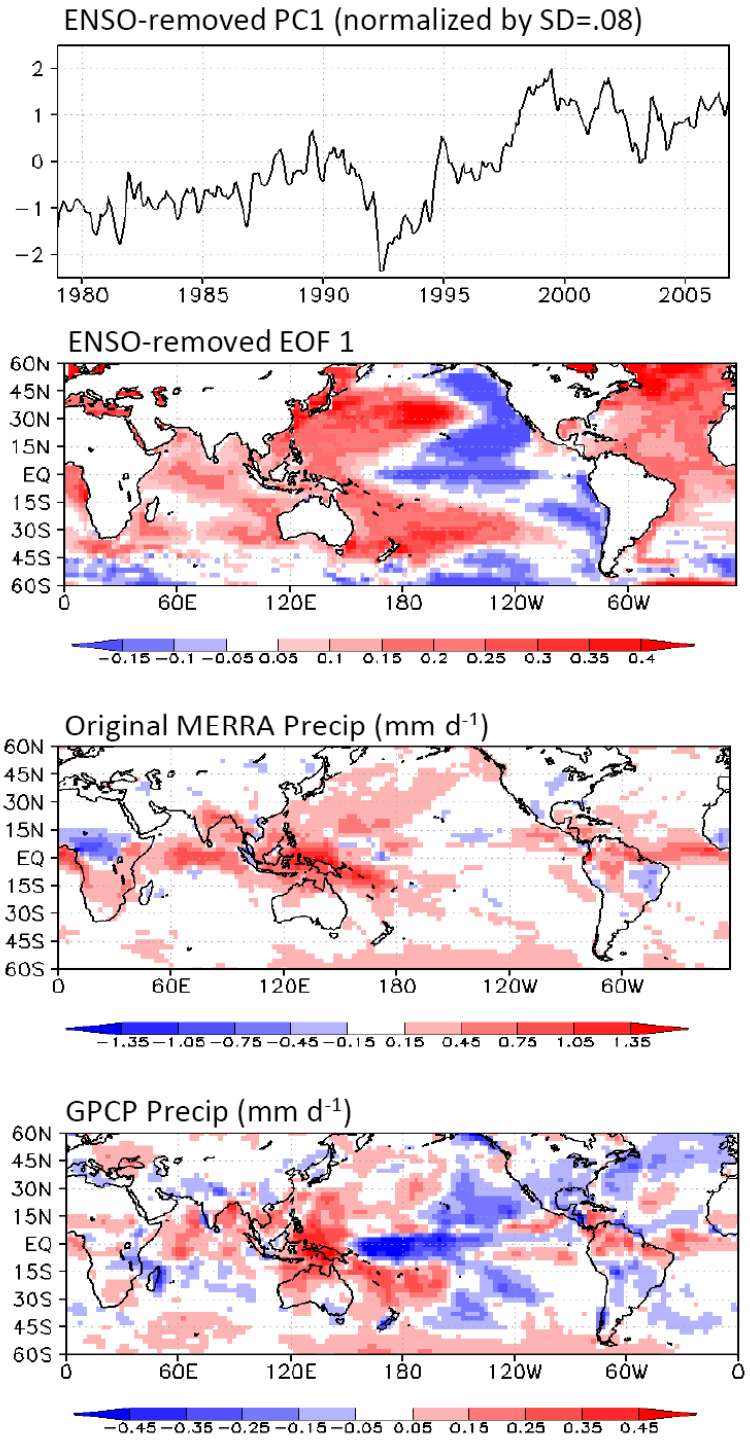

Figure 10. The leading SST PC (normalized) and EOF after the global ENSO signals have been removed. Original MERRA and GPCP precipitation regressed against PC1 with units of mm d^{-1}. See text for details on the methodology.

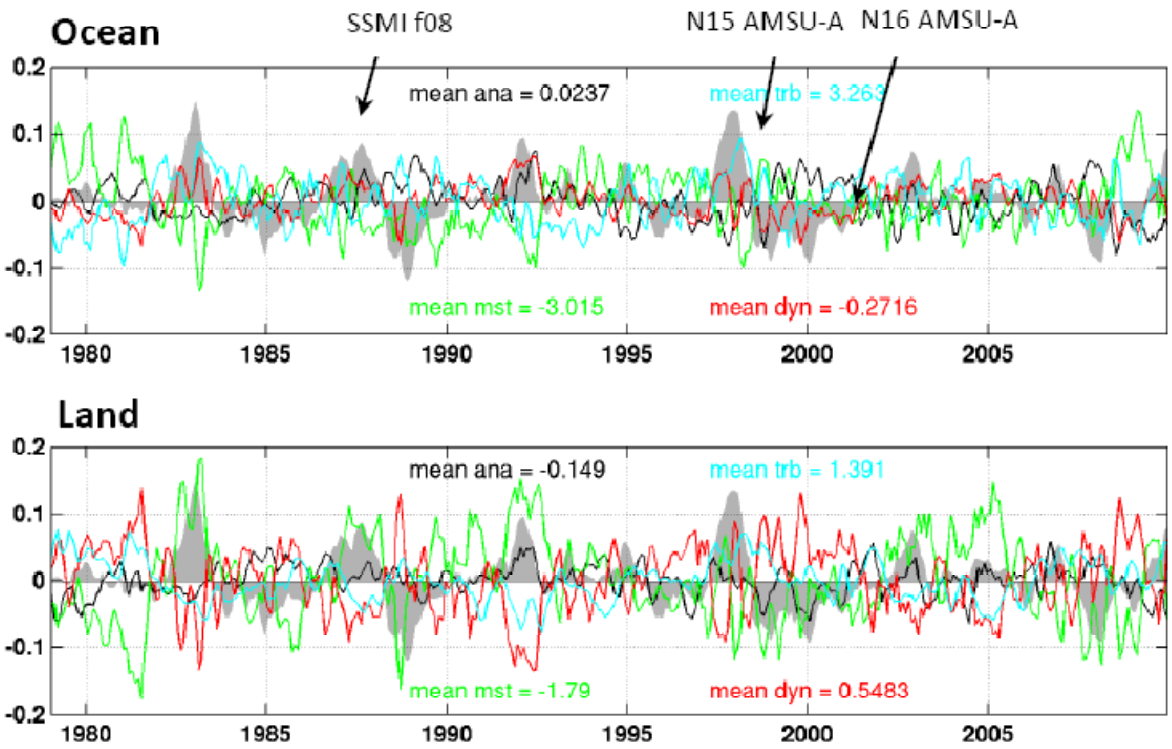

925
926 Figure 11. Global ocean and land area-average moisture budget anomalies (mm day^{-1}) after PCR
927 removal of artifact signals. Budget terms are: Moist processes ≅ precipitation (green),
928 evaporation (cyan), vertically-integrated moisture flux convergence (red) and moisture increment
929 (black). Anomalies are departures from monthly mean climatological mean values over the
930 1979-2009 period which are also noted in their appropriate color. Shaded curve is Nino 3.4 SST
931 anomaly x 0.05.
932
933

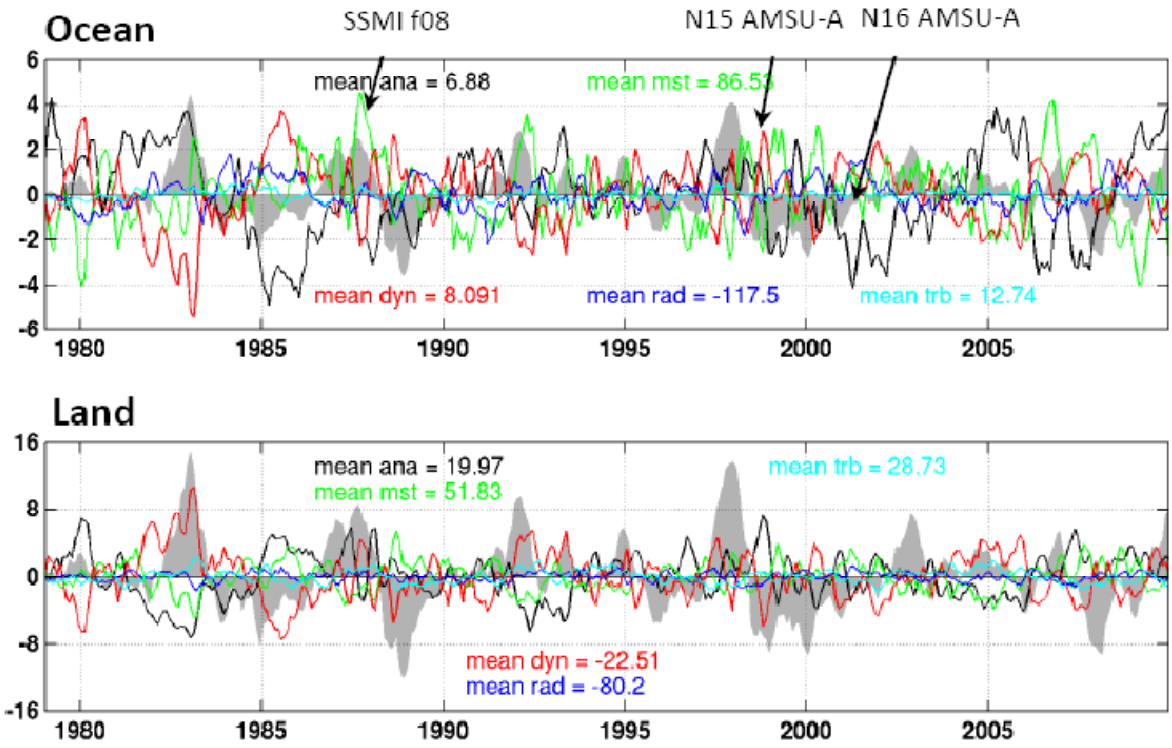

Figure 12. Same as Figure 11 but for enthalpy budget. Units are W m^{-2}. Time series of heating anomalies by moist processes (green), dynamics (red), radiative processes (blue), dynamical processes (red), turbulence or sensible heat flux (cyan), and analysis increment (black) are plotted with the climatological mean values also shown in their respective colors. Shaded curve is Nino 3.4 SST anomaly x 1.5 (over ocean) and x 5.0 (over land).

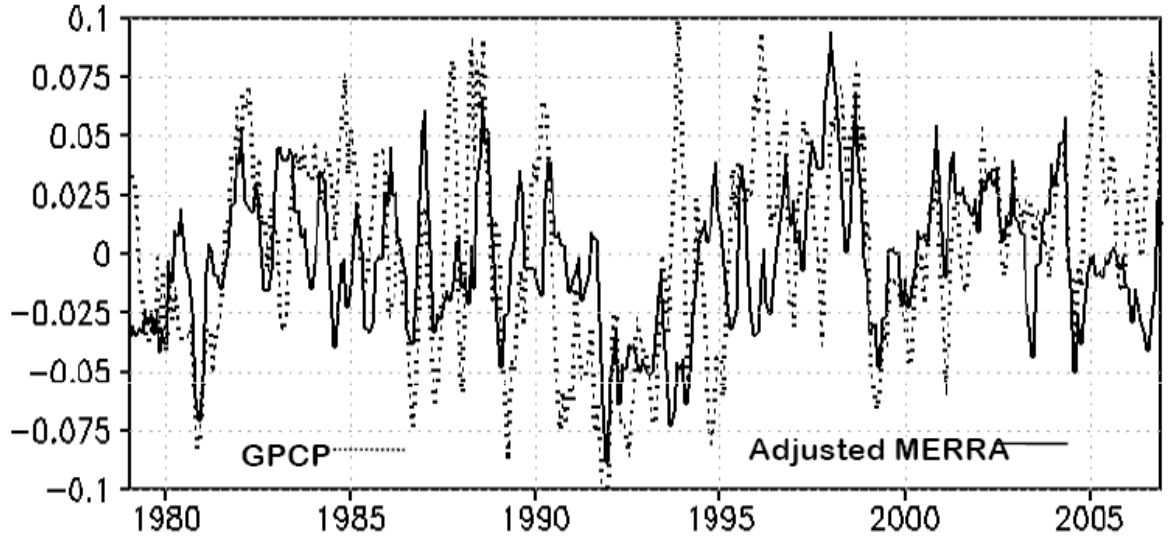

941
942 Figure 13. The quantity $P_q^* \equiv -1.0 \times (MST_q + ANA_q)$ averaged over the globe +/- 60^o (black)
943 compared to GPCP precipitation (dotted). Units are mm d^{-1}.

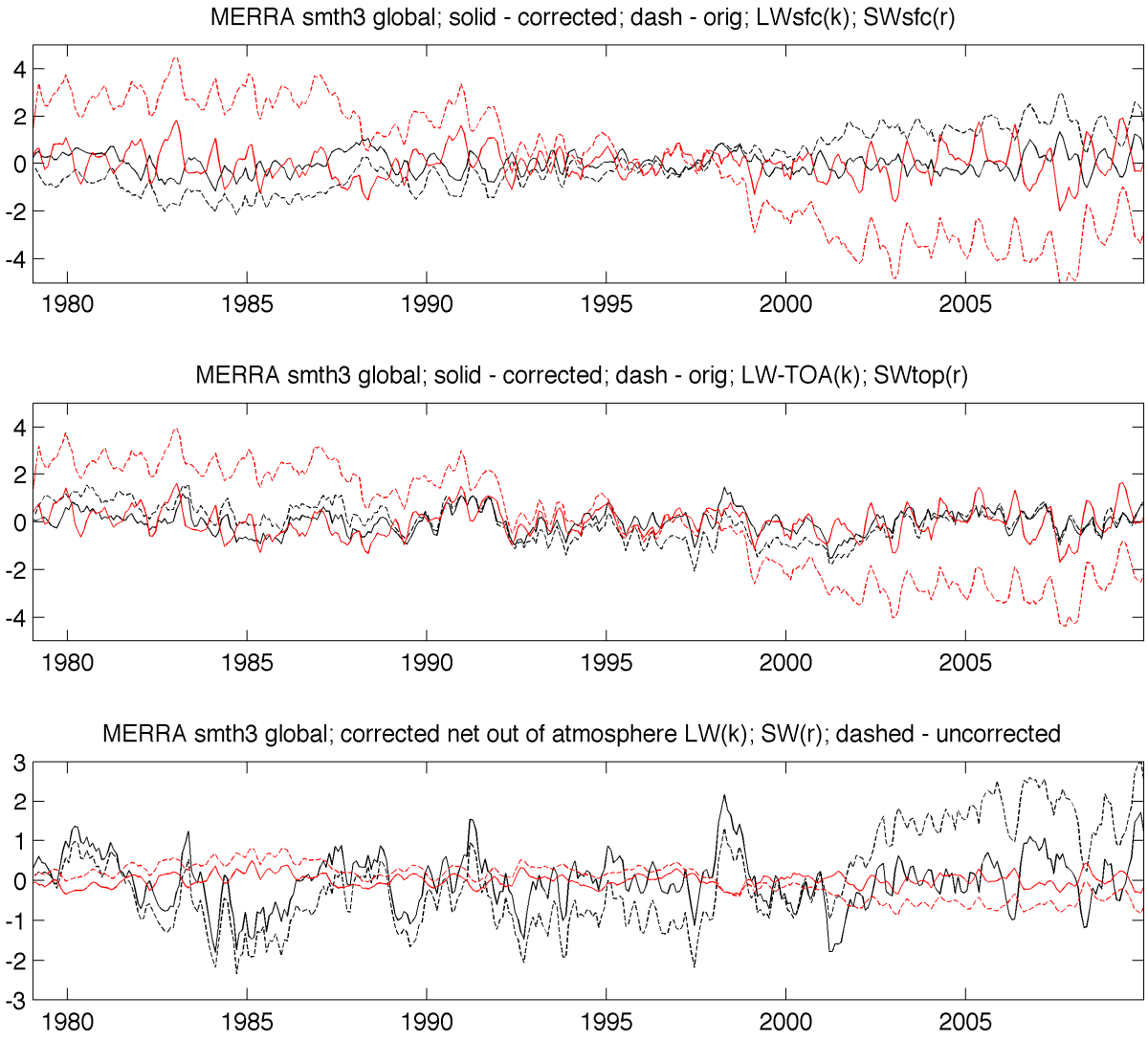

Figure 14. Radiative flux components (Wm^{-2}): original (dashed) and corrected (solid). Top: Surface net LW (black) and net SW(red). Middle: TOA OLR (black) and net SW (red). Bottom: Net atmospheric cooling by LW (black) and SW (red).

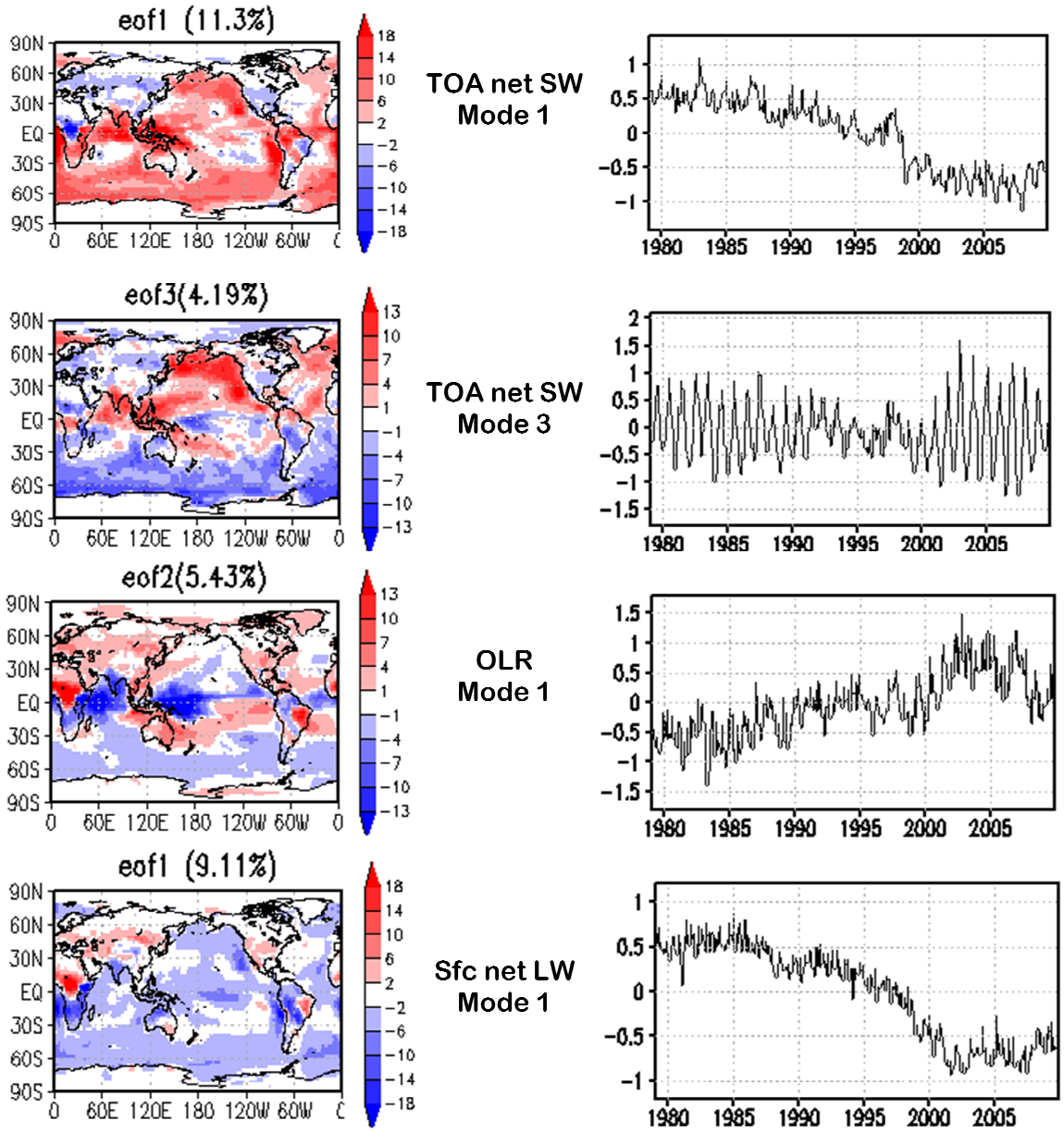

Figure 15. Selected EOFs and PCs from analysis of individual component fluxes. PCs are normalized so that EOFs carry the units of Wm^{-2}.

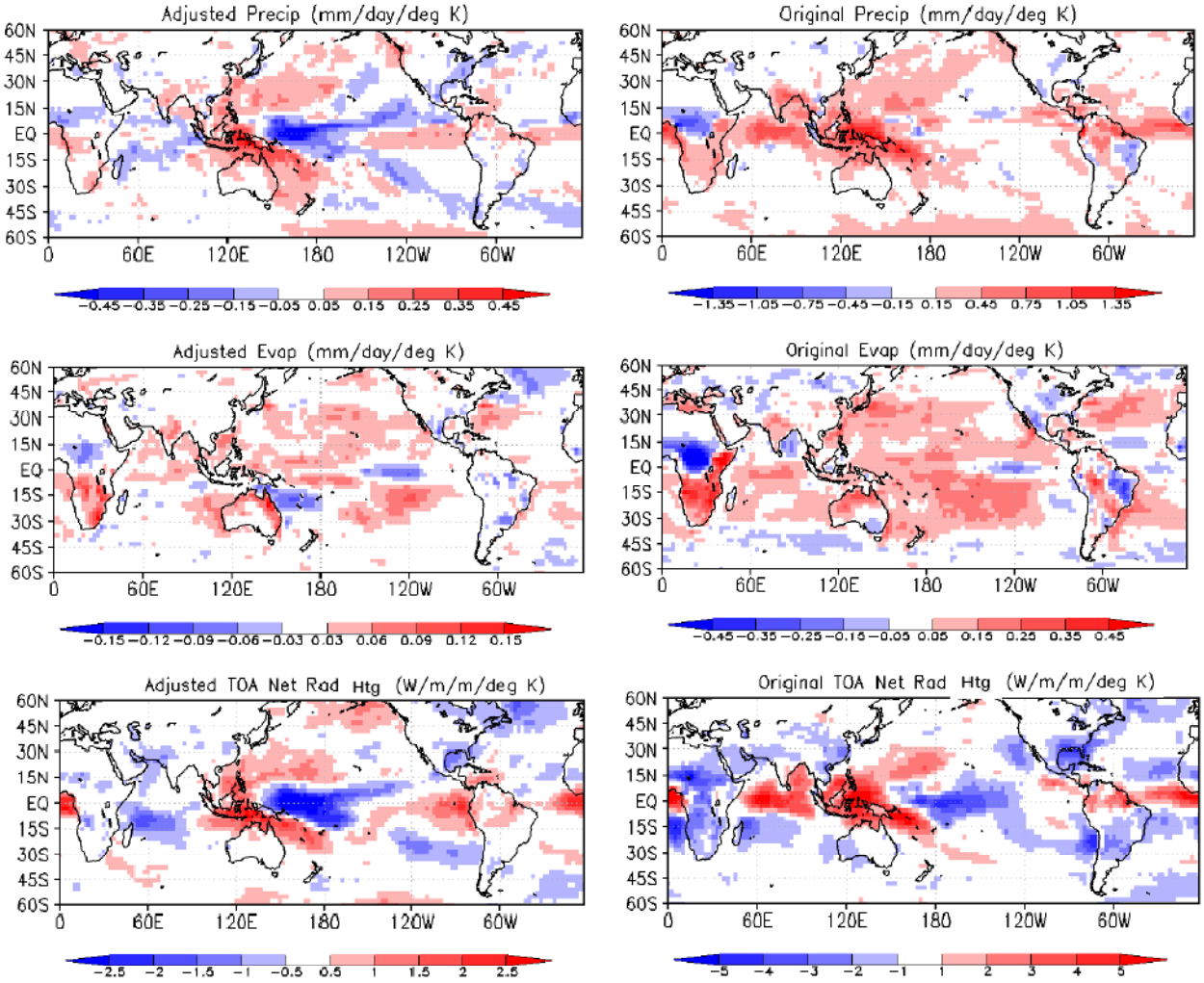

Figure 16. Adjusted and original regression maps of MERRA fluxes on the PC in Figure 9: (Top) precipitation, mm d^{-1}; (Middle) evaporation, mm d^{-1}; (Bottom) net atmospheric radiative heating, Wm^{-2}.